Preprint Title	A cantilever-based, ultra-high vacuum, low temperature scanning probe instrument for multidimensional scanning force microscopy
Authors	Hao Liu, Zuned Ahmed, Sasa Vranjkovic, Manfred Parschau, Andrada-Oana Mandru and Hans J. Hug
Publication Date	09 Jun 2022
Article Type	Full Research Paper
ORCID® iDs	Hao Liu - https://orcid.org/0000-0003-3211-1007

A cantilever-based, ultra-high vacuum, low temperature scanning probe instrument for multidimensional scanning force microscopy

Hao Liu*[1,2], Zuned Ahmed*[1,2], Sasa Vranjkovic[1], Manfred Parschau[1], Andrada-Oana Mandru[1] and Hans J. Hug[1,2]

Address: [1]Empa, Swiss Federal Laboratories for Materials Science and Technology, CH-8600 Dübendorf, Switzerland and [2]Department of Physics, University of Basel, CH-4056 Basel, Switzerland

Email: Hao Liu - hao.liu@empa.ch; Zuned Ahmed - zuned.ahmed@empa.ch

* Corresponding author

Abstract

Cantilever-based atomic force microscopy (AFM) performed under ambient conditions has become an important tool to characterize new material systems as well as devices. Current instruments permit robust scanning over large areas, atomic scale lateral resolution and the characterization of various sample properties using multifrequency and multimodal AFM operation modes. Research of new quantum materials and devices however, often requires low temperatures and ultra-high vacuum (UHV) conditions. In this article, we describe a cantilever-based low temperature UHV AFM setup that allows to transfer of the versatile AFM techniques developed for ambient conditions to UHV and low temperature conditions. We demonstrate that such a cantilever-based AFM offers experimental flexibility by permitting multimodal or multifrequency operations with superior force derivative sensitivities and bandwidths. Our instrument has a sub-picometer gap stability and can simultaneously map not only vertical and lateral forces with atomic-scale resolution, but also perform rapid overview scans with the tip kept at larger tip-sample distances for robust imaging.

Keywords

atomic force microscopy; ultra-high vacuum; atomic resolution; multimodal operation; instrumentation design

Introduction

Atomic force microscopy (AFM) operated under vacuum or ultra-high vacuum (UHV) conditions is beneficial for increasing measurement sensitivity, measuring samples at low temperatures [1], analyzing reactive surfaces [2] and studying atomic or molecular adsorbents with atomic or submolecular resolution [3]. First AFM images with true atomic resolution were obtained by using cantilever-based AFM instruments, where cantilevers with stiffness on the order of few tens of Newtons per meter were oscillated with amplitudes of a few nanometers [4-7]. Atomic resolution is achieved if the tip-sample distance is sufficiently reduced, such that an overlap of atomic orbitals between tip apex atom and atoms at the surface can occur. In recent years, functionalizing tip apex with a low coordinated atom/molecule resulted in exceptional submolecular resolution at low temperature [8-11].

Tuning fork AFM has become increasingly popular for atomic resolution work performed under UHV conditions [12]. In tuning fork AFM, one of the prongs of the tuning fork is fixed to the tip holder, while the other one acts like a macroscopic cantilever. The comparatively large dimensions of the prongs facilitates the attachment of a small but macroscopic wire tip to the free prong. Compared to the typically-used microscopic AFM cantilevers, the tuning fork sensor has a rather high stiffness $k \sim 2\,\mathrm{kN/m}$. This facilitates AFM operation with small oscillation amplitudes ($A < 100\,\mathrm{pm}$) because a snap-to-contact or instabilities of the phase-locked loop (PLL) driving the tuning fork oscillation do not occur. Furthermore, the tuning fork AFM does not require an extra deflection sensor such like the beam deflection or fiber optical systems used for cantilever-based AFM, thus substantially reducing instrumentation complexity. In fact, every existing scanning tunneling microscope (STM) can be transformed into tuning fork-based AFM simply by replacing the rigid STM tip by a tuning fork with an attached tip and by adding an extra pre-amplifier and a

PLL to drive the tuning fork oscillation and measure shifts in its resonance frequency arising from the tip-sample interaction. However, because of the macroscopic size of the tuning fork, the high stiffness of the sensor goes together with a low resonance frequency typically around 30 kHz. This substantially limits the minimally-measurable tip-sample interaction force gradients such that very small AFM measurement bandwidths (typically below 10 Hz [13]) must be used, leading to extremely long measurement time for three-dimensional force volume maps. For example, the 3D frequency shift map acquired in the work of Albers et al.[14] with a volume of $1.6 \times 0.8 \times 0.12\,\mathrm{nm}^3$ and 256 × 119 × 61 pixels has required a total acquisition time of 40 h, i.e. was measured with a pixel bandwidth of only 12.9 pixels per second.

While to date most atomic resolution studies under UHV conditions are performed with tuning fork-based AFM, the vast majority of the AFM work performed under ambient conditions rely on microfabricated cantilevers that are able to detect with various mechanical properties and tips. Microfabricated cantilevers can be optimized for different AFM applications and operational environments. For AFM performed under ambient conditions, microfabricated cantilevers can, for example, be operated in different oscillation modes [15] or at multiple frequencies [16-23] to simultaneously map different sample properties. Further, the high resonance frequency of microfabricated cantilevers combined with high-bandwidth cantilever deflection detection permits video-rate scanning [24], real-time peak force detection [25] or a later artificial intelligence processing of the vast amounts of data acquired during imaging [26,27]. Under vacuum conditions, the beneficial resonance frequency-to-stiffness ratio of low-thickness cantilevers proved to be beneficial for the measurement of ultrasmall forces [28] or, in combination with high cantilever quality factors, the detection of small magnetic fields [29]. For the latter, new tip-sample distance control operation modes were developed which again relied on multifrequency techniques [30-33]. Such multimodal and multifrequency techniques have also been applied for AFM work performed under UHV conditions, for example, to measure atomic scale forces in different special directions [34-36] or to work with sub-nanometer oscillation amplitudes for an improved detection of short-ranged inter-atomic forces [37-39].

Despite the success of AFM utilizing microfabricated cantilevers under ambient conditions, early work performed under UHV conditions and high-sensitivity MFM under vacuum conditions, cantilever-based AFM has lost the attention of the surface science and UHV AFM communities, possibly because of the ease of operation of tuning fork-based AFM and the availability of the corresponding instruments from various manufacturers. Here, we present the design of a robust and easy-to-use cantilever-based AFM instrument, which is not only optimized for atomic resolution work, but also permits high bandwidth AFM operation, and thus at least in principle, the implementation of more complex AFM operation modes (typically used for ambient environment AFM) also under UHV and low temperature conditions. We further demonstrate that this instrument can be used for multimodal AFM operation, for example to simultaneously map vertical and lateral forces and tunneling current signals with atomic resolution, but also permits the measurement of weak forces with high measurement bandwidths permitting the acquisition of overview images at larger tip-sample distances. Our instrument is thus well-suited to find specific locations in devices, map weak magnetic or electrostatic forces, also permits the acquisition of smaller scan range atomic resolution images at specific locations.

This manuscript is organized as follows: the UHV and cryosystem are described in section II, which is followed by the microscope design outlined in section III. A fiber optical interferometer system is used as deflection sensor (section IV) and it permits the simultaneous detection of flexural and torsional cantilever oscillation modes for multidimensional AFM measurements. The performance of the instrument is discussed in section V, starting with an analysis of the relevant AFM noise sources, continued by a presentation of the obtained measurement bandwidths and tip-sample gap stability. Various atomic scale STM and AFM results are then described in section VI, demonstrating the performance of our new AFM for such work. Section VII finally summarizes all results.

UHV Chambers and Cryosystem

The UHV system [40] consists of a cryostat chamber and a preparation chamber with an attached load-lock as shown in Fig. 1. The preparation chamber is equipped with various ports for the attachment of evaporators, a sputter gun and surface science analytical tools. A rotatable coolable linear manipulator with two sample/cantilever receivers are used to transport sample and cantilever holders to the different positions of the preparation chamber and finally, to transfer to the cryostat chamber. For the transfer of the sample/cantilever holders from the load-lock system to the linear manipulator inside the preparation chamber and then from the linear manipulator to the corresponding receivers in the microscope, customized magnetic feedthrough manipulators with hex-key end-pieces are used.

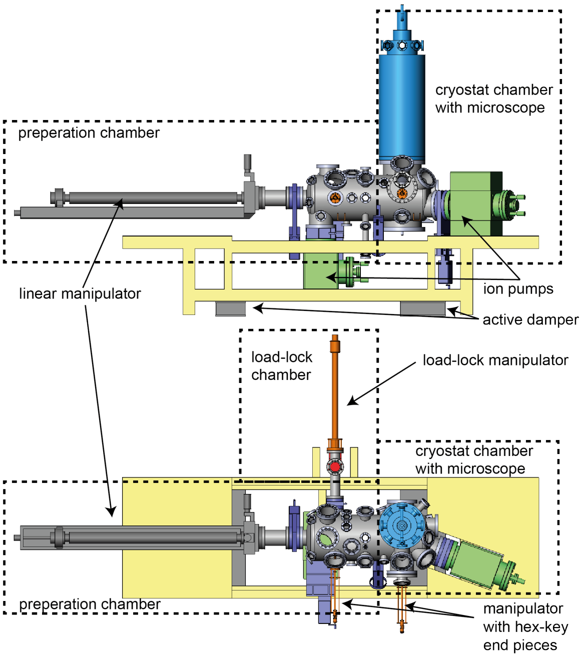

Figure 1: CAD drawings of the top and side views of the UHV system consisting of a cryostat chamber, a preparation chamber and a load-lock chamber.

The cryostat and preparation chamber are both pumped with 300 l/s ion pumps, which also include titanium sublimation sources. The load-lock chamber is pumped with a 67 l/s turbo pump. The bath cryostat manufactured by Cryovac [41] is mounted on top of the cryostat chamber outside the long axis of the chamber system [Fig. 1]; this permits a rapid transfer of (precooled) sample/cantilever holders from the manipulator to the microscope .

The liquid Helium (LHe) tank of the cryostat is surrounded by a liquid Nitrogen (LN_2) container and an additional heat shield that is passively cooled by the evaporating He gases of the LHe tank [Fig. 2(a)]. The microscope is surrounded by two shields: an inner one mounted on the LHe cryostat bottom plate, and an outer one that is connected to the bottom of the surrounding LN_2 tank. With this construction, standby times of 80 hours for the LHe and 96 hours for the LN_2 tank are obtained.

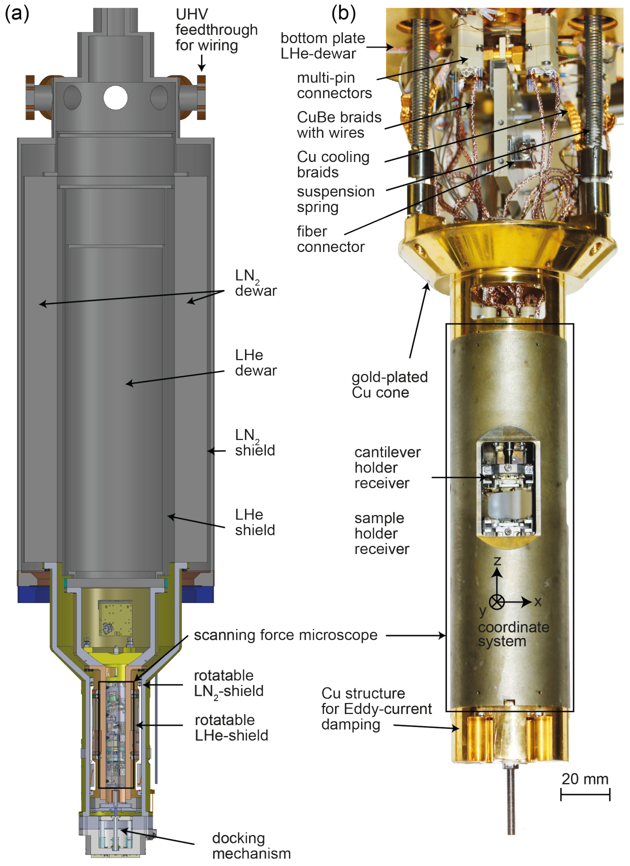

Figure 2: (a) The bath cryostat consists of two tanks: the inner tank holds 8 liters of LHe and the outer tank holds 19 liters of LN_2, additionally with their own shields. The microscope is attached to the cone and hanging freely on three suspension springs as shown in the photograph (b).

The scanning force microscope is attached to a Cu cone (hangs on three suspension springs) that reach through cylindrical tubes running through the LHe tank, and are mounted on top of the tank. Together with the Eddy current damping system mounted at the bottom of the cryostat, this provides excellent vibration isolation such that a tip-sample gap stability better than 1 pm can be obtained on a normal laboratory floor and with operation personnel in the same room. Note that all experiments discussed in section VI have been performed with personnel in the room.

The heat transfer between the microscope and the Cu bottom plate of the LHe of the cryostat is achieved through the electrical connections between the microscope and the connectors on the cryostat bottom plate together with the gold coated Cu braids that connect the Cu cone to the cryostat bottom but keep a high mechanical flexibility [Fig. 2(b)]. Note that for the electrical connections between the connectors on the cryostat bottom plate and feedthroughs of the UHV system, low-heat-conductive phosphor bronze wires [42] are used. The wires run down along the LHe tank with several attachment points to further reduce the heat flow from the room temperature UHV flange connectors to the cryostat bottom plate. For the Cu braids, in order to permit a defined grounding of the microscope, independent of that of the UHV system, the Cu braids are electrically insulated through a sapphire plate from the cryostat bottom plate. For a more rapid cooling, the microscope can be pulled down by a LN_2-cooled pulley system that locks in at the microscope bottom such that a mechanical contact between the Cu cone and the cone shaped part of the LHe microscope shield is achieved.

To obtain access to the microscope, the LN_2 shield can be rotated such that it connects to the inner LHe shield to open up an access window to the microscope for sample and cantilever holder transfer. The cantilever, the optical fiber and the sample can be seen at a large optical viewing angle permitting a good microscopic view required for the positioning of the fiber relative to the cantilever. This allows for example the positioning of the fiber end outside the long axis of the cantilever to measure torsional cantilever oscillation modes (see section IV) or the approach of the sample to the (cantilever) tip. An additional position of the shields opens a small access hole to the sample surface permitting the deposition of atoms or molecules on the cold sample.

Microscope Design

We use a fiber-optical interferometer to measure the cantilever deflection. This deflection sensor type only requires placing the end of an optical fiber in close proximity to the cantilever, but all electronic components remain outside the cryostat and the UHV system. Moreover, a fiber-optical interferometer sensor directly maps the cantilever deflection, whereas beam-deflection sensors only measure the angular change of the cantilever [43]. A fiber-optical interferometer thus permits a precise measurement of the cantilever oscillation amplitude, without the need of a complicated calibration [44-46]. Fiber optical sensors can obtain sensitivities up to about 1 fm/$\sqrt{\text{Hz}}$ using Fabry-Pérot interferometry [47,48]. To date, we however only implemented a simpler form of the interferometer and having a cleaved and uncoated fiber end with a reflectivity of typically 4 %. This limits the sensitivity of the interferometer to about 89 fm/$\sqrt{\text{Hz}}$, (see section VI for the characterization of the interferometric deflection sensor).

Figure 3(a) shows a typical setup for a UHV STM or tuning fork-based AFM. Preferably, the low-mass tip is scanned, while the heavier sample and sample receivers are mounted on a xy-stage for the lateral positioning of the sample on a millimeter scale. To avoid stacking the z-motor on top of the xy-positioning unit, the xyz-scan piezo and tip-receiver unit are mounted inside a z-positioning unit, permitting the approach of the tip to the sample. Typically, the shear-piezo plates used for the stick-slip positioners are mounted on the instrument body, while a slider contains the scan piezo [13].

In a cantilever-based AFM, the deflection sensor (here a cleaved fiber end) must be positioned relative to the cantilever. Scanning the cantilever tip would be impractical in this case, because it would require scanning the entire fiber positioning unit as well as the cantilever. Instead, the cantilever remains fixed to the instrument body, the fiber end is positioned on top of the cantilever, and the sample is scanned relative to the cantilever. This setup, on the other hand, requires stacking of the z-positioner on top of the xy-positioning unit or vice-versa, making the design of a mechanically rigid instrument more challenging. In addition, the mass of the sample holder and sample holder receiver must be kept to a minimum in order to keep the resonance frequency of the xyz-scan piezo

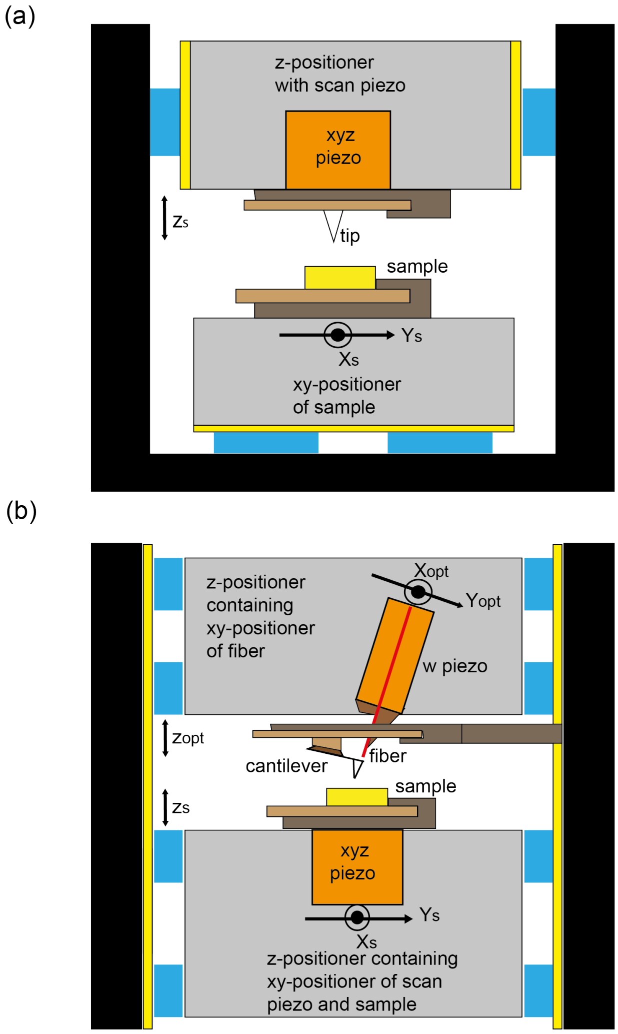

Figure 3: Schematics of the components of (a) a typical, classical STM / tuning fork-based AFM setup with the tip being scanned and (b) our AFM with the sample being scanned.

reasonably high, as required for a fast feedback. Furthermore, to avoid instrument downtime due to piezo tube fractures, sample exchange inside the UHV must be performed with minimal force applied to the scan piezo. The schematic setup of our instrument is displayed in Fig. 3(b). Our cantilever-based AFM instrument is made of two three-axis piezo-motor modules that position (A) the sample versus the cantilever tip (sample positioning unit) which is equipped with a sample scan-piezo, and (B) the fiber versus the cantilever back-surface (fiber positioning unit) which contains a piezo (w-piezo) for fine-tuning the fiber-to-cantilever distance and for keeping the interferometer at one of its most sensitive operating points.

Sample positioning unit

For the sample positioning unit, Pan style piezo-motors [49] are used. Triangular voltage pulse trains are applied to all shear piezo stacks simultaneously. In order to minimize the instrument volume and to maximize its mechanical rigidity, the scan piezo is integrated into the xy-positioning unit that is contained inside the z-positioning unit which moves inside the instrument body. Different to conventional z-positioning units, as for example used in the work of Schwenk et al.[13] and Hug et al.[50], here the shear piezo stacks are attached to the sliding unit. This is one of the many design steps we have undertaken to improve the stability of the tip-sample gap: because the shear piezos move together with the z-positioner containing the scan piezo with the sample, the mechanical loop from the tip to the sample becomes small in the approached state, whereas in the classical design [Fig. 3(a)], the shear piezos are attached to the body of the instrument leading to the largest mechanical loop in the approached state.

A further advantage of this design is that the instrument body can be manufactured as a single piece, in the form of a cylindrically-shaped tube [Fig. 4(a)]. As a result, only the sapphire plates, but not the piezo-stacks, need to be glued on the inside walls of the body.

Our design with the piezos attached to the moving part however requires a spring system that applies a force from the inside towards the sapphire plates mounted on the inside of the instrument's body tube [Fig. 4(a) and (b)]. Figure 4(c) and (d) show the top and side views of the z-positioning unit containing the xy-positioning unit and the xyz-scan piezo carrying the sample receiver. While four of the six shear piezo stacks are glued to the z-slider unit, the two remaining stacks are glued to a leaf-spring assembly depicted in Fig. 4(a) and (b). The central screw (red arrow) pushes the leaf-spring against two support cylinders, leading to an outward motion of the piezo stacks, pressing them against the sapphire rail (wide red arrows). With the screw in its released position, the sample z-positioning unit (and also that of the fiber which is not shown in Fig. 4) can be placed inside the cylindrical body tube [blue arrow in Fig. 4(a)] and the shear piezo stacks can be pressed towards the sapphire rails by tightening the adjustment screw that is accessible through a hole in the cylindrical instrument body.

The z-positioning units of the sample and fiber also contain the corresponding xy-positioning units. To avoid any cross-coupling of the xy-motion as observed in earlier designs [50], two separated units with confined motions in the x- and y-directions are used here [Fig. 4(d)]. Such a stacking of two linear positioning units on top of the z-positioning units in a small building space however imposed various design challenges: first, a high mechanical rigidity must be obtained for a good tip-sample gap stability; secondly, the mechanical loop must be minimized and the design has to be kept as symmetrical as possible to reduce thermal drift; thirdly, the design must allow a precise adjustment of the pressure of the sliders towards the sapphire rails for the xy-directions.

All these conditions can be fulfilled with a concentric design, where the shear-stacks of the x-positioning unit are attached close to the top of the z-sliding unit [Fig. 5(a)]. The x- and y-sliders both use three shear stacks and confine the motion along these directions by sliding an Al_2O_3 sphere attached to the shear stack inside a gap formed by two sapphire cylinders. The shear stacks for the x-direction are glued to the inside close to the top surface of the z-slider [Fig. 5(a)]. The x-slider is then arranged below these stacks and contains the three shear stacks of the y-direction which then move the y-slider. The xyz-piezo is then attached to the top of the latter reaching through a hole in the x-slider to the top of the z-slider, such that the sample holder receiver is sufficiently high that the sample holder can be introduced into it. Both sliders are then pressed against their piezo stacks using a single three-armed leaf spring at the bottom with a sapphire sphere running on a hardened steel plate. The sphere is contained in a cage mounted to a fine-thread, and a screw is used to adjust the force acting on the shear stacks of both the x- and y-sliders, facilitating the setting of a force sufficiently large to have a rigid assembly, but small enough to move the sliders at low temperatures, where the range of the shear stacks is significantly reduced.

With this concentric design, dimensional changes in the height of the shear stacks and sliders with temperature are at least partially compensated by those of the scan piezo. Together with the highly symmetric design along the x and y axes, this further reduces the thermal drift. Moreover, a wiggling motion of the size δ (for example arising from a mechanical excitation of the spring suspension system of the microscope) of the x-sliding plate away from the supporting shear piezo stack

[Fig. 5(b)], will translate into a later motion of $\delta/2$ [Fig. 5(c)] much smaller than the mechanically amplified motion of $\delta \cdot \frac{L_z}{L_x}$ occuring in the classical stacked xy-motor design depicted in Fig. 5(d) and (e).

Fiber positioning unit

The same type of z- and xy-positioning units are also used to approach the fiber to the cantilever backside and to position it along and perpendicular to the cantilever axis. Note that the xy-positioners for the fiber are tilted by the same 12 ° angle [Fig. 6] as the cantilever to permit the y-positioning of the fiber parallel to the long axis of the cantilever. Similar to xy-positioners of the sample, the x- and y-positioners of the fiber can be independently adjusted without any cross-coupling. This permits a reliable positioning of the fiber either above the central axis of the cantilever or towards the cantilever edges to pick up torsional cantilever deflections (see section IV). In order to maximize the sensitivity of the interferometric cantilever deflection measurement, a fiber-to-cantilever distance between two adjacent interference extrema must be selected and kept constant. This fine-positioning is performed by the w-piezo stack [Fig. 6].

Sample and cantilever holders

UHV AFM instrumentation typically permits the in-situ exchange of samples and (cantilever) tips. For this, the sample and cantilever are mounted on corresponding holders [Figs. 7(a)-(c) and (d)-(f), respectively]. For efficient UHV AFM experimental work, it is favorable to have a conveniently large number of different sample and cantilever holders. Such holders with electrical contacts, on the other hand, are complex and their fabrication and assembly typically require considerable efforts. For this reason, all our sample/cantilever holders use the same four laser-cut metal parts as base plates (m1-m4) connected via a simple ceramic center piece [Fig. 7(f)] on top of which different assemblies can be arranged, for example, to carry a sample button heater [Figs. 7(a)-(c)] or a shaker piezo for the mechanical excitation of the cantilever oscillation [Figs. 7(d)-(f)].

Sample and cantilever receivers

These sample/cantilever holders can be transported through the UHV system using the linear manipulator. In most instruments, the receivers for the sample or cantilever holders use clamping springs to fix the holders in their positions [Fig. 7(g)]. However, the introduction of the sample/cantilever holder into the corresponding receiver requires overcoming frictional forces which may lead to a deformation of the holding springs and, consequently, to a loose fixation of the sample/cantilever holder in its receiver. Moreover, the sliding motion will also create wear particles which may contaminate the surface of the sample or the inside of the instrument. Generally, such receiver designs compromise between a sufficiently large clamping force and the frictional forces which need to be overcome to exchange the sample/cantilever.

Here, we designed a new type of sample/cantilever receivers containing an adjustable clamping spring to overcome these inherent problems [Fig. 7(h)]. When the sample/cantilever holder is introduced or removed from the receiver, the clamping spring is in a lower position, not touching the sample/cantilever holder, such that the latter can be introduced or moved without applying forces to the receiver. The fixation of the sample/cantilever holder is then performed by rotating the fixation screw, which pushes the clamping spring against the sample/cantilever holder [Fig. 7(h)]. The required rotary motion can be applied via a customized magnetic-feedthrough manipulator which includes a rotatable hex-key end piece [Fig. 7(i) and (j)]. This end piece can further be moved along its axis, permitting the clamping of a sample/cantilever holder and thus allows its safe and rapid transport between the linear manipulator head and the corresponding receivers in the AFM [Fig. 7(k)].

Note that we have tested different designs for the screw-activated clamping mechanism. We found the mechanism to be reliable (permits operation for more than a year with lots of sample/cantilever holder exchanges) with a conical screw coated by dichronite running in a thread of the receiver [fixation screw and thread piece in Fig. 7(h)]. The screw or the part with the thread can easily be replaced in the case of extensive wear. The conical end of the screw then presses on a sapphire inlay glued to the bottom part of the clamping spring.

The fixation of the sample/cantilever holder inside the corresponding receiver also leads to an electrical contact between pads on the sample/cantilever holder and contact pins on the receiver. We typically use three (out of the four) contact pins on the holder top, but can also use two contact pins on the clamping springs and hence have a total of 5 electrical contacts. Because four top contacts overdefine the plane of the sample/cantilever holder, the holder typically has a smaller thickness in one of the front contact areas, such that only one of the front electrical pins makes contact with the holder. A modified design of our holder with more (spring-loaded) electrical contacts from the top has been recently described by Schwenk et al.[13].

Modular wiring design

In order to facilitate instrument service, modification or repair, every module of the microscope has a separate wiring branch and can thus be easily removed from the microscope without having to remove wires or connectors from the module.

For the sensitive signal inputs and outputs, such as STM current and sample bias voltage, coaxial cables Lakeshore CC-SS-100 [51] with a SMA connector at their ends are used. These are wired to the two front electrical contact pins [Fig. 7(d) to (f)]. For all other contacts and also the wiring for the scan piezo, piezo motors, piezo for the mechanical actuation of the cantilever oscillation, temperature sensor (below the sample holder) and heaters, silver coated Cu wires (DABURN 2451 [52]) are used. For electrical screening, wires carrying opposite voltages (X+ and X-, Y+ and Y- for the scanner as well as W+ and W- for the w-piezo) are twisted. Furthermore, groups of twisted pairs are contained in a CuBe braid with a home-built multi-pin connector at the end, which is then plugged into the corresponding connector receiver on the bottom plate of the LHe tank of the cryostat [Fig. 2(b)].

From the multi-pin connector receiver at the cryostat bottom, the wire-bundles for specific instrument modules are reordered into functional groups, e.g. a group containing all wires for the piezo positioners, sample scan and w-piezo, electrical contacts to the sample and cantilever and instrument heaters and temperature sensors.

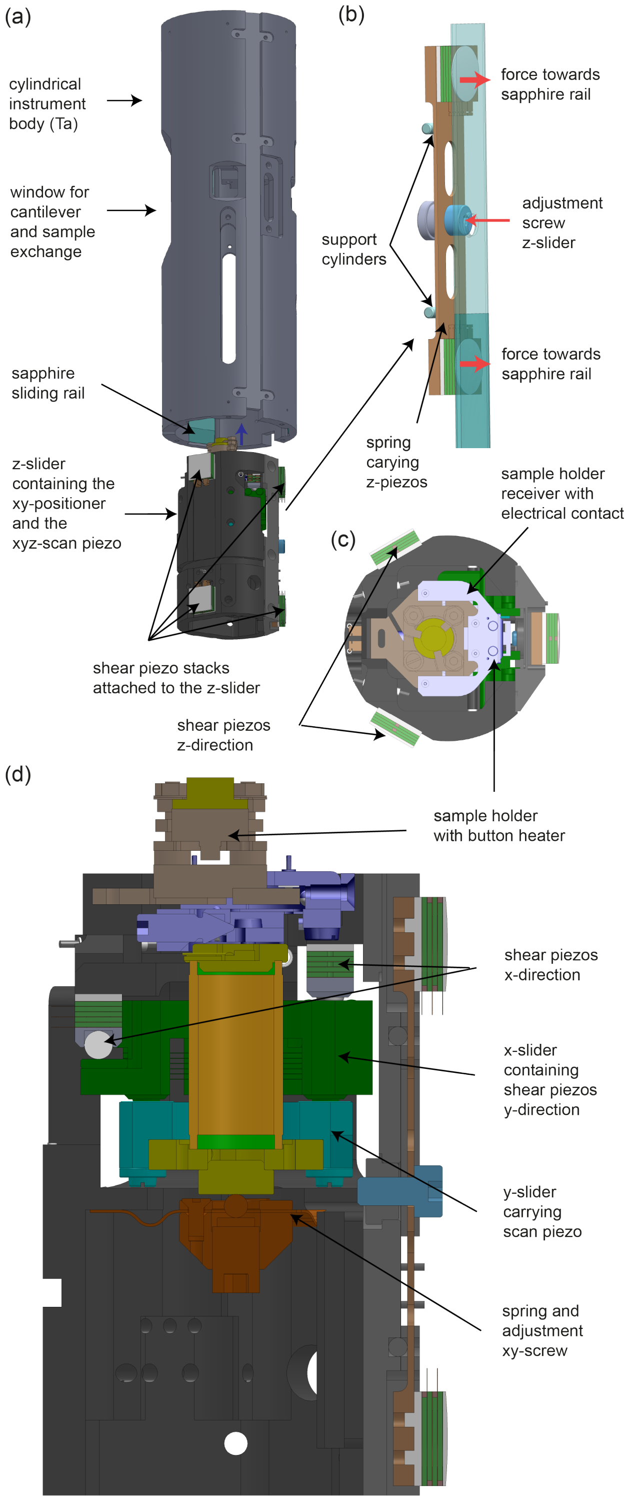

Figure 4: CAD drawings of the cylindrical body tube (a) and the leaf spring (b) carrying two of the total of six z-piezo shear stacks. The top and the cross-scetional views of the z-slider unit are shown in (c) and (d), respectively. The z-positioning unit also contains the xy-positioning unit and the xyz-scan tube carrying the sample holder receiver with the sample holder.

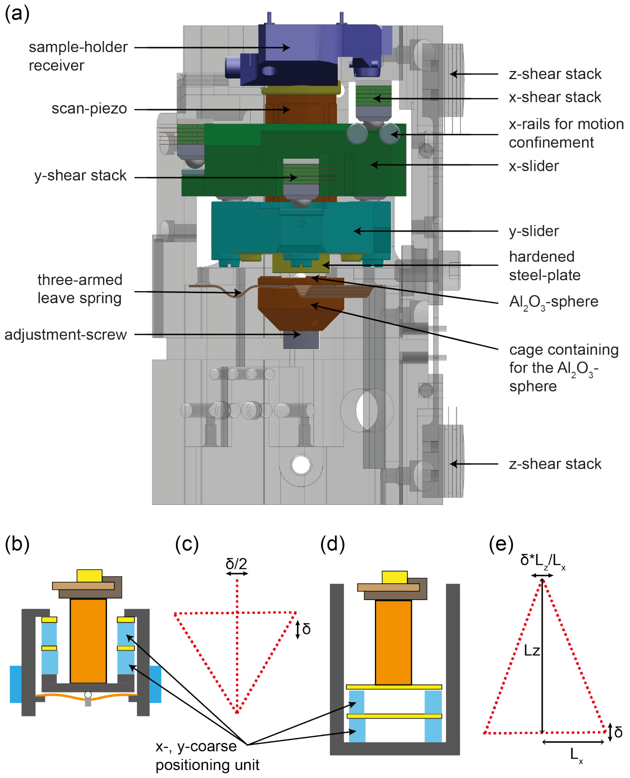

Figure 5: (a) CAD drawing of the z-positioning unit containing the xy-positioning units with scan piezo and mounted to it the sample holder receiver. (b) schematic drawing of the assembly depicted in (a) highlighting the concentrical design, and (c), the corresponding stability triangle. (d) schematic drawing of a more conventional design, where the scan piezo is mounted on the top of the xy-positioning unit, and (e), the corresponding stability triangle.

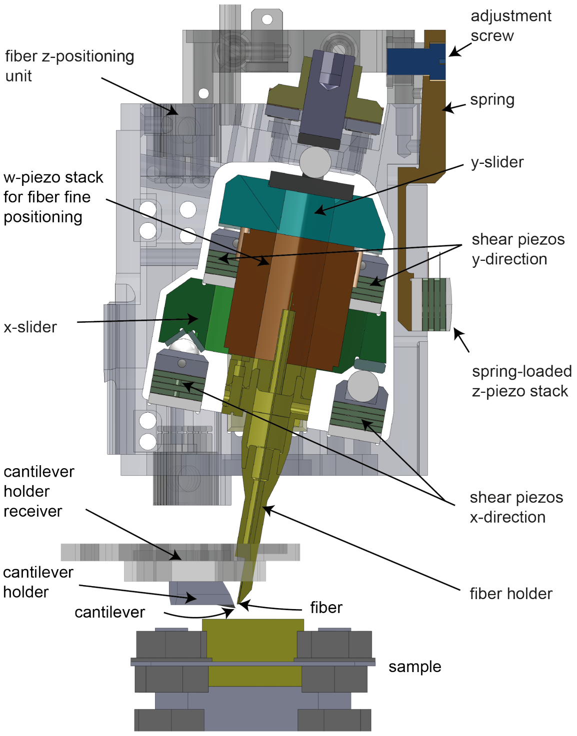

Figure 6: CAD sketch of the fiber z-positioning unit containing the x- and y-positioning unit. The assembly can be placed inside the cylindrical instrument body. After tightening the adjustment screw, the spring-loaded z-shear piezo stack and consequently the z-shear piezo stack attached to z-positioning unit will be pressed towards the sapphire rails on the inside of cylindrical instrument body. The cantilever-to-fiber geometrical configuration is also highlighted. The cantilever and the fiber are tilted by 12 ° relative to the sample.

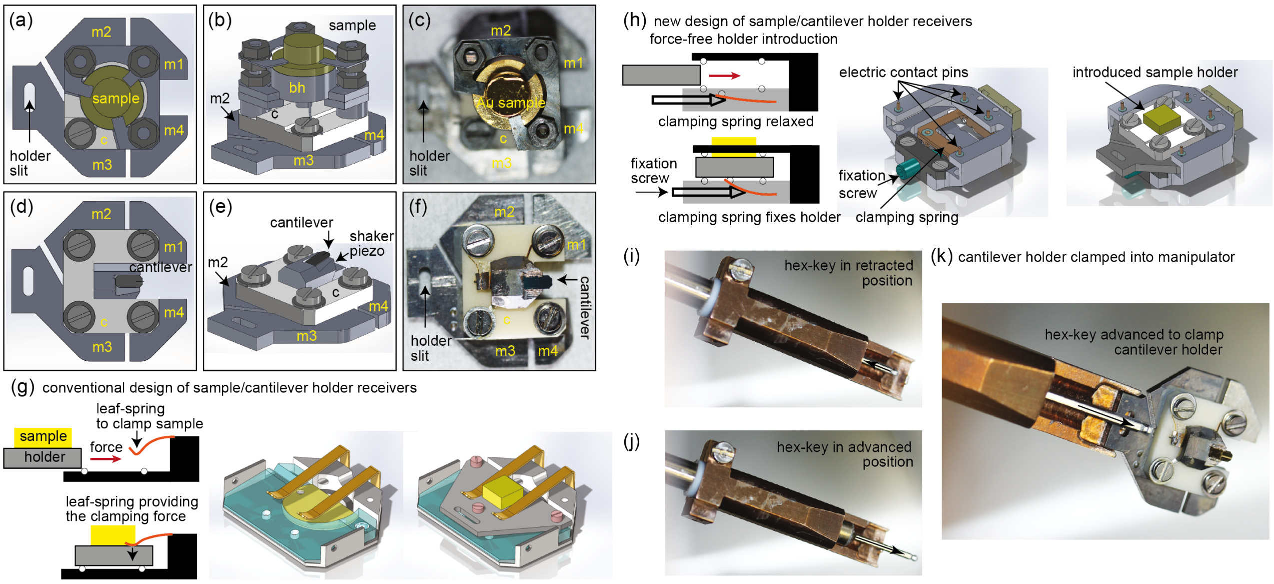

Figure 7: (a) and (b) top and side view CAD sketches of a sample holder with a button heater for sample preparation. (c) a hat-shaped Au(111) single crystal mounted in a sample holder containing a button heater. (d) and (e) top and side view CAD sketches of a cantilever holder with a shaker piezo integrated into the holder below the cantilever. (f) a cantilever holder with a mounted (glued) cantilever. The wire on the top-right to the m1 contact plate is for the measurement of the tunneling current. The wire on the top-left contacts the cantilever shaker piezo, while the wire on the bottom left provides the ground and shields the cantilever excitation voltage from the cantilever. (g) typical sample/cantilever receiver design used in earlier instruments [46] where the sample/cantilever holder are clamped down by springs. (h) new sample/cantilever receiver design used here, permitting a force-free introduction/removal of the sample/cantilever from the corresponding receiver. (i) and (j) manipulator with a rotatory hex-key end piece that can be moved along its long axis to clamp a sample/cantilever holder for a safe transport between the chamber transport system and the sample/cantilever holder receiver in the AFM (k).

Interferometer system

The layout of the fiber optical interferometer system is depicted in Fig. 8(a). To perform the interferometry, we use a Sony SLD201 V3 laser diode with a wavelength of 785 nm coupled via an optical insulator to a Au-coated monomode optical fiber having a core diameter of 5 μm [53] delivering a maximum of 9.3 mW into the fiber at a drive current of 140 mA. To keep the temperature of the laser diode constant, it is mounted onto a Thorlabs TCLDM9 [54] thermoelectric cooler block and the laser diode is operated at constant current. A combined laser diode and temperature controller (Thorlabs ITC502 [54]) controls both the current and the temperature. In contrast to earlier designs which relied on a 50:50 fiber-optical 2×2-coupler, the increased power of the laser diode permits [44,45] the use of a 98:2 fiber-optical $2{\times}2$-coupler with the laser diode connected to one of the two 2 % branches. Thus, for the 9.3 mW maximum input power, only 1.4 %, i.e. 127 μW reaches the fiber end in the AFM, because of additional losses in the optical connectors. This minimizes the light coupled to UHV/cryostat system (blue shaded area in [Fig. 8(a)]) containing the AFM and thus a potential heating effect, but maximizes the intensity of the light reflected back from the fiber-end /cantilever assembly to the measurement photo-diode, which leads to about 50 μW on the measurement photodiode that is part of a 10 MHz bandwidth current-to-voltage converter.

The interferometer system can be equipped with an additional laser diode (LP633-SF50 [54]) with a wavelength of 635 nm coupled into the fiber with the 2-color-combiner (NR73A1 [54]) allowing an optical excitation of the cantilever oscillation. We found that a mechanical excitation of the higher cantilever oscillation modes can become challenging if other resonances arising from the mechanical setup of the cantilever holder with its excitation piezo are located close to the cantilever resonance. Figures 8(b) and (c) show the measured amplitude and phase of the second flexural cantilever resonance excited mechanically (by the shaker piezo on the cantilever holder), or optically (using a DC- and AC-current for the 635 nm laser diode to oscillate its light intensity), respectively. Note that the additional color-filter placed in front of the photodiode prevents the backreflected 635 nm light to reach the photodiode, such that only the interference of the 785 nm laser light is used to map the cantilever deflection. For the specific cantilever, the dependence of the amplitude and phase on excitation frequency expected for a harmonic oscillator becomes disturbed significantly by a nearby mechanical resonance of the cantilever holder for a mechanical excitation of the cantilever [Fig. 8(b)]. Because the cantilever resonance frequency changes the cantilever interacts with the surface, i.e. in AFM operation mode, the 180° phase shift from the cantilever resonance can overlap with the phase shift arising from the mechanical resonance, leading to a failure of the phase-locked loop to track the cantilever's resonance frequency. In such a case, optical excitation is preferred. In contrast to the mechanically-excited cantilever, an optical excitation leads to an ideal harmonic oscillator behavior [Fig. 8(b) and (c)].

Note that the 10 MHz bandwidth of the photodiode current-to-voltage converter permits the measurement of higher flexural and torsional modes occurring at frequencies well beyond 1 MHz [Fig. 8(d)]. To measure torsional cantilever oscillation modes, the fiber needs to be positioned outside the long-cantilever axis, close to the boundary of the cantilever [55]. Figure 8(e) shows the measured interferometer signal as a function of the fiber position across the cantilever. For a cantilever width w of 30 μm, we can estimate the laser spot size to be about 10-15 μm on the cantilever. Figure 8(f) shows the measured size of the first flexural (red curve, left vertical axis) and torsional (blue curve and right vertical axis) cantilever oscillation mode with frequencies of 2.959 kHz and 2.206 MHz as a function of the position of the fiber across the cantilever. While the flexural mode oscillation signal [red curve in Fig. 8(f)] remains roughly constant [with a slight dip in the middle of the cantilever similar to that observed in the interference signal from Fig. 8(e)], the torsional mode signal vanishes at the center of the cantilever [blue curve in Fig. 8(f)]. The absence of the signal at the center of the cantilever can also serve as a signature to clearly identify a torsional oscillation mode.

Performance of the SPM

Relevent AFM noise sources

Microfabricated low mass cantilevers offer considerable advantages concerning measurement noise, measurement bandwidth and further permit multimodal AFM operation schemes [56], at the

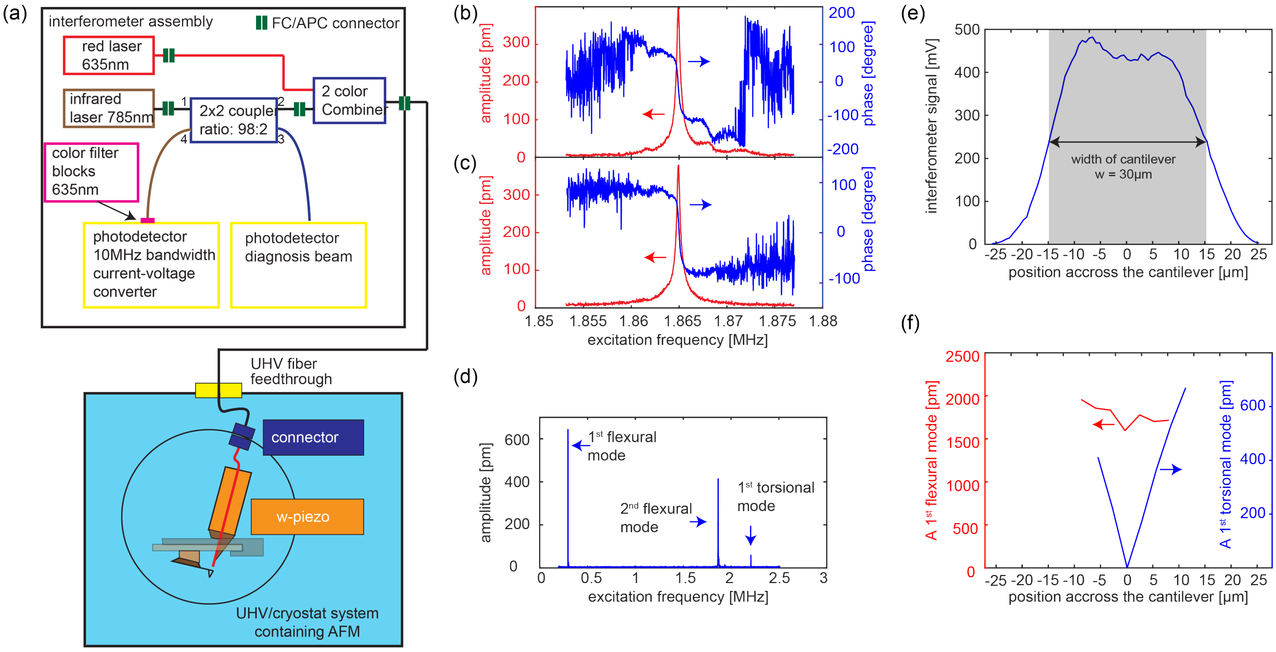

Figure 8: (a) setup of the interferometer system. (b) and (c) amplitude and phase as a function of the frequency for mechanical and optical cantilever excitation, respectively. (d) wide frequency range mechanical excitation spectrum of the cantilever showing the first and second flexural and first torsional resonances. (e) interferometer signal as a function of the fiber position across the cantilever (displayed schematically by the gray area). (f) measured oscillation amplitudes of the cantilever for the first flexural (red) and first torsional oscillation modes (blue), respectively. The torsional oscillation modes vanish if the fiber is positioned above the central axis of the cantilever.

cost of an increased complexity of the instrumentation arising from the need of an additional deflection sensor which needs to be positioned relative to the cantilever. As discussed by Kobayashi et al.[57], the measurement noise arises from three different noise sources, i.e. thermal noise of the cantilever (thermal noise), noise of the deflection sensor (deflection noise) and noise arising from fluctuations of the oscillator circuitry driving the cantilever oscillation (oscillator noise). These noise sources all limit the minimally-measurable rms z-derivative of the z-component of the force, as given by the expressions:

$$\left.\frac{\partial F_z}{\partial z}\right|_{\mathrm{th}} = \frac{1}{A_{\mathrm{rms,i}}} \cdot \sqrt{\frac{4k_{\mathrm{B}}Tk_iB}{2\pi f_iQ_i}} \propto \sqrt{\frac{k_i}{f_iQ_i}} \ , \tag{1}$$

$$\left.\frac{\partial F_z}{\partial z}\right|_{\mathrm{def}} = \frac{1}{A_{\mathrm{rms,i}}} \cdot \frac{n_{\mathrm{eq}}2k_iB^{\frac{3}{2}}}{\sqrt{3}f_i} \propto \frac{k_i}{f_i} \ , \tag{2}$$

$$\left.\frac{\partial F_z}{\partial z}\right|_{\mathrm{osc}} = \frac{1}{A_{\mathrm{rms,i}}} \cdot \frac{n_{\mathrm{eq}}k_i\sqrt{B}}{Q_i} \propto \frac{k_i}{Q_i} \ , \tag{3}$$

where: k_i, f_i, Q_i, and $A_{\mathrm{rms,i}}$ are the stiffness, free resonance frequency, quality factor, and rms oscillation amplitude of the i-th cantilever oscillation mode (different flexural or torsional oscillation modes),respectively; $k_{\mathrm{B}} = 1.38 \cdot 10^{-23}\ \mathrm{JK}^{-1}$ is the Boltzmann constant, T is the temperature, B is the bandwidth at which the measurement is performed, and n_{eq} is the noise of the deflection sensor, given in units of $\mathrm{m}/\sqrt{\mathrm{Hz}}$. The minimally-measurable rms z-derivative of the z-component of the force then arises from the sum of all noise sources and is thus given by:

$$\left.\frac{\partial F_z}{\partial z}\right|_{\mathrm{tot}} = \sqrt{\sum_{i=\mathrm{th,def,osc}} \left.\frac{\partial F_z}{\partial z}\right|_i^2} \ . \tag{4}$$

For rectangular cantilevers, the flexural modal stiffness and resonance frequency of the i-th flexural oscillation modes are related to the first flexural mode stiffness and resonance frequency, respectively, by:

$$k_i = k_1 \cdot \left[\frac{\alpha_i}{\alpha_1}\right]^4 \ , \tag{5}$$

$$f_i = f_1 \cdot \left[\frac{\alpha_i}{\alpha_1}\right]^2 \ , \tag{6}$$

$$\tag{7}$$

where $\alpha_i = \{1.8750, 4.6941, 7.8548, ...\}$ are coefficients defined by the characteristic equation of an oscillating rectangular cantilever with one free end [58]. Note that for a typical non-contact

AFM experiment, the tip end of the cantilever can be considered as free because the cantilever force constant is generally much smaller than the measured derivative of the tip-sample interaction force [59]. The force constant of a rectangular cantilever and its first flexural mode stiffness, respectively are given by:

$$c_{\mathrm{L}} = \frac{E_{\mathrm{Si}} t^3 w}{4L^3} \quad \text{and} \quad k_1 = \frac{c_{\mathrm{L}} \alpha_1^4}{12} \ , \tag{8}$$

where: $\rho_{\mathrm{Si}} = 2331\,\mathrm{kg/m^3}$ and $E_{\mathrm{Si}} = 1.69 \cdot 10^{11}\,\mathrm{N/m^2}$ are the density and elastic modulus of silicon, respectively; L, w, and t are the length, width and thickness of the cantilever, respectively. While the first two geometrical dimensions are well-defined by the fabrication process and can easily be measured by electron microscopy, the thickness t of the cantilever is best obtained from the measured first mode flexural resonance frequency f_1 using:

$$t = \frac{2\pi f_1 L^2}{\alpha_1^2} \cdot \sqrt{\frac{12\rho_{\mathrm{Si}}}{E_{\mathrm{Si}}}} \ . \tag{9}$$

The expressions for the minimally-measurable force derivative (eq. 1 and eq. 2) arising from thermal and deflection sensor noise, respectively, reveal that a high quality factor (for a low thermal noise) and a a low modal stiffness resonance frequency ratio (for both noise sources) are beneficial for a high signal-to-noise ratio or large measurement bandwidths. Because the stiffness depends on $\frac{t^3}{L^3}$ (eq. 8), whereas the resonance frequency is proportional to $\frac{t}{L^2}$ (as derived from eq. 9), a low stiffness-to-frequency ratio at a reasonably high resonance (several tens or hundreds of kHz) is best obtained with low-thickness microfabricated cantilevers. A small cantilever thickness is further beneficial for the support loss quality factor (which is one of the relevant energy loss terms), because $Q_{\mathrm{support}} \propto 1/t^3$ [60].

The measurement of magnetic, electric or van der Waals forces is thus best done with low thickness cantilevers. These cantilevers typically have resonance frequencies of a few tens of kHz (comparable to that of a tuning fork) but a stiffness that is about four orders of magnitude smaller than that of a tuning fork, resulting in a reduction of the thermal and deflection noise by two and four orders of magnitude (see table 1) assuming the same quality factor. Note that, for a soft cantilever, the deflection noise obtained with typical deflection sensors is negligible such that thermal noise is dominant. Recently, Feng et al.[29] have demonstrated that at room temperature a force derivative of 78 nN/m is detectable in a 1 Hz-bandwidth, which is of particular importance for the measurement of small magnetic forces and for MFM with optimized lateral resolution.

To perform atomic resolution, cantilevers with a higher stiffness are required to meet the stability criteria:

$$c_\mathrm{L} > -\left.\frac{\partial F_\mathrm{ts}}{\partial z}\right|_\mathrm{max} , \tag{10}$$

or

$$c_\mathrm{L} \cdot A > |F_\mathrm{ts}|_\mathrm{max} , \tag{11}$$

where F_ts is the tip-sample interaction force. From eq. 10, the cantilever stiffness must surpass the highest attractive force gradient acting on the cantilever to prevent a snap to contact. Alternatively, such a snap-to-contact can also be prevented by a sufficiently large cantilever oscillation amplitude, such that the restoring force surpasses the maximum attractive force (eq. 11). Further, sufficient energy must be stored in the cantilever oscillation. To obtain an oscillation energy of a few tens of electron volts at smaller cantilever oscillation amplitudes, e.g. $A = 100\,\mathrm{pm}$, typically force constants of a few hundred N/m are required. This permits a stable oscillation of the cantilever and tracking of the resonance frequency shifts, even in the presence of energy loss processes arising from stochastic changes of atomic positions at the tip apex or sample atoms interacting with the tip [61]. Such stiffnesses are typically obtained in the second flexural oscillation mode of cantilevers with a first flexural mode stiffness of a few tens of N/m (eq. 5). While the second modal stiffness of such cantilever has about the same order of magnitude as that of a tuning fork, its resonance frequency is almost two orders of magnitude higher. According to eqs. 1 and 2, cantilever sensors have thermal and deflection noise advantage of about one and two orders of magnitude under the assumption that the quality factor and noise of the deflection sensor can be compared to those of a tuning fork. Moreover, the deflection noise (eq. 2) depends on the 1.5-th power of the bandwidth, whereas the thermal noise (eq. 1) depends on the square root of the measurement bandwidth. For a hard cantilever and likewise for a tuning fork sensor, the deflection noise can become the dominant noise source, such that a low stiffness-to-resonance frequency ratio becomes particularly relevant.

Note that the oscillator noise (eq. 3) solely depends on the deflection noise, the cantilever stiffness and the quality factor. Hence, having a high resonance frequency is not beneficial. However, as Kobayashi already pointed out [57], the oscillator noise is not relevant for a high-Q-cantilever, provided that the thermal noise peak is sufficiently larger than the noise of the deflection sensor, i.e. the thermal noise amplitude at the corner frequencies, $f_{c_{1,2}} = f_0 \pm \frac{f_0}{2Q}$, is considerably larger than the background noise of the deflection sensor. This is typically fulfilled for the first and second flexural and first torsional oscillation modes of microfabricated cantilevers, such that the oscillator noise contribution is negligible. Table 1 summarizes the stiffness-to-frequency ratios for typical microfabricated cantilevers and tuning forks. According to eqs. 1 and 2, these ratios determine the minimally-measurable force derivative or for the obtainable measurement bandwidth (measurement speed).

As it becomes apparent from Table 1, a cantilever-based AFM offers high measurement sensitivities, and permits advanced multimodal or multifrequency operation modes. Moreover, cantilevers with a wide range of stiffnesses, resonance frequencies and tips are available, allowing for the selection of a cantilever that is best suited to a certain measurement situation.

Force gradient noise and measurement bandwidths

Figure 9(a) shows thermal noise data measured at 6.4 K of a Nanosensors PPP-NCHPt cantilever having $L = 125\,\mu$m, $w = 30\,\mu$m and a measured first mode resonance frequency $f_0 = 295.97$ kHz, together with the fitted resonance curve and the detector noise of our currently implemented interferometer (which is 89 fm/$\sqrt{\text{Hz}}$ for the non-coated, cleaved fiber end used here). Note that at such

Table 1: Thermal and detector noise sensitivities of different cantilevers and oscillation modes normalized to that of a tuning fork (TF in the table) sensor (higher numbers, i.e. higher measurement sensitivities are better). Line 1: high-quality factor MFM cantilever operated under vacuum conditions [29] in its first flexural mode. Lines 2 and 3: typical cantilever used for atomic resolution work, operated in the first and second flexural mode, respectively. Line 4: tuning fork sensor [13] operated in its flexural mode for comparison with lines 1-3. Line 5: For bi-axial force gradient measurements with a tuning fork [62], its length extension mode was used to map the vertical force gradient. Line 6: again displays the cantilever with the properties given in line 3, but now compared to the sensitivity of the tuning fork length extension mode given in line 5. Line 7 then shows the lateral force sensitivity obtained with the first torsional oscillation mode of a cantilever (that can be measured simultaneously with its second flexural mode, line 3) which needs to be compared to the sensitivity of the tuning fork operated in its conventional flexural mode (line 4).

		k [N/m]	f_0 [kHz]	Q [k]	$\sqrt{\frac{k}{f_0 Q}}$ [normalized]	$\frac{k}{f}$ [normalized]
measurement of vertical force gradient						
1	MFM 1st flex	0.5	50	250	129.10	6667
2	AFM 1st flex	25	300	100	28.29	800
3	AFM 2nd flex	982	1’880	10	3.57	127
4	TF flex	2’000	30	100	1	1
simultaneous measurement of vertical and lateral force gradients						
5	TF l.ext	1.43M	567’000	N/A	N/A	1
6	AFM 2nd flex	982	1’880	10	N/A	4831
7	AFM 1st tors	500	220’000	20	7.67	293

laser powers, the cantilever quality factor is increased or decreased by photothermal effects such that two different quality factors are measured for the interferometer working points on the rising and the falling slopes of the interferometer signal [63-65]. Figure 9(b) displays the two different resonance curves with an enhanced (red curve) and attenuated quality factor (blue curve) measured at a lower laser power than the resonance curve displayed in Fig. 9(a) with quality factor further attenuated by the higher laser power down to the 91k, as obtained from the fit of the resonance curve. The quality factor relevant for the thermodynamic cantilever noise would be obtained at even lower laser powers than that used to measure the resonance curves displayed in Fig. 9(b), can be approximated by the mean of the two quality factors, i.e. $Q_1 = \frac{Q_1^{\mathrm{enh}} + Q_1^{\mathrm{att}}}{2} \approx 100\mathrm{k}$. Note that the quality factor of the second flexural mode is not noticeably influenced by the interferometer operation point, but is typically considerably lower, $Q_2 \approx 10\mathrm{k}$ than Q_1. We attribute this to energy dissipation arising by instabilities of the atomic positions of atoms inside the grain boundaries [66] of the rather thick metallic coating applied to the tip side of the cantilever. Note that the coating is required to

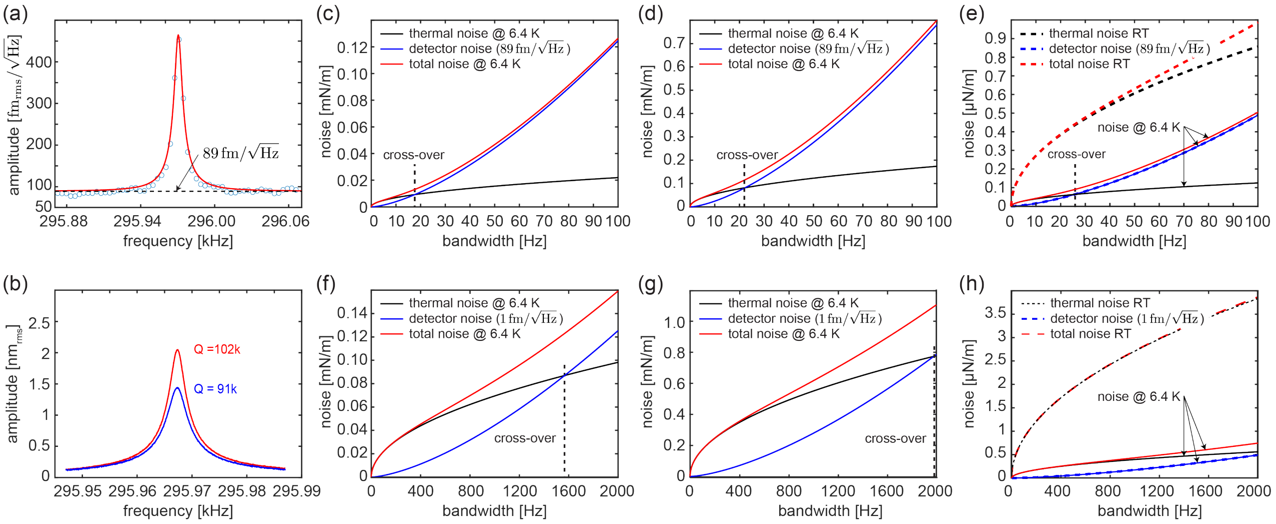

Figure 9: (a) narrow band thermal noise spectrum of a NCHPt cantilever with a length $L = 125\,\mu$m and width $w = 30\,\mu$m around the cantilever first mode flexural resonance. The fitted resonance frequency and interferometer noise floor are $f_0 = 295.95$ kHz, and 89 fm/$\sqrt{\mathrm{Hz}}$, respectively. (b) The measured quality factors on the two interferometer slopes are $Q_{\mathrm{damp}} = 91$ k and $Q_{\mathrm{exc}} = 102$ k. (c) and (d) force derivative thermal, detector and total noise in mN/m for the first and second flexural oscillation mode at $T = 6.4$ K, an oscillation amplitude $A = 100$ pm, and a detector noise floor of 89 fm/$\sqrt{\mathrm{Hz}}$, where $k_1 = 25.2$ N/m, $k_2 = 1005$ N/m, $f_1 = 295.95$ kHz, $f_2 = 1865$ kHz, $Q_1 = 100$ k, and $Q_2 = 10$ k. (e) noise data (here in μN/$\sqrt{\mathrm{Hz}}$) for $T = 6.4$ (solid lines) and $T = 300$ K (dashed lines) for the first flexural mode of an MFM cantilever [29] with a first mode resonance frequency $f_1 = 51$ kHz, first mode stiffness of 0.86 N/m, an rms-oscillation amplitude of $A = 5$ nm, and a first mode quality factor $Q = 242$ k. At higher bandwidths, i.e. at 18 Hz (1st mode), 22 Hz (2nd mode), and 25 Hz (MFM cantilever at $T = 6.4$ K), the detector noise becomes the dominant noise source. Panels (f)-(h) display the noise results for bandwidths up to 2000 Hz extrapolated from (c) to (e) for a detector noise floor improved to 1 fm/$\sqrt{\mathrm{Hz}}$ as for example reached by Refs. [47] and [48] with different types of fiber-optical Fabry-Perét interferometers.

permit tunneling, but the coating thickness along the cantilever could presumably be minimized using masking procedures similar to those used for the coating of high-quality factor cantilevers for magnetic force microscopy [29]. In future work, much thinner coating thicknesses could be used, or the coating could be applied to the cantilever side to reduce energy dissipation processes arising from the grain boundaries of the polycrystalline coating.

The cantilever thickness $t = 3.352\,\mu$m using eq. 9 measured first flexural mode resonance frequency $f_1 = 295.95$ kHz [Fig. 9(a)], and the length $L = 125\,\mu$m and width $w = 30\,\mu$m given by the manufacturer. Using eqs. 8, 5, and 6, the force constant $c_{\mathrm{L}} = 24.4$ N/m, the first flexural mode stiffness $k_1 = 25.2\,\mathrm{N/m}$, second flexural mode stiffness $k_2 = 1005\,\mathrm{N/m}$, and the second flexural mode resonance frequency $f_2 = 1865\,\mathrm{kHz}$ can be obtained. Note that the second mode resonance frequency calculated from eq. 6 typically differs from the measured second mode resonance frequency by only a few percent. The noise of the interferometer deflection measurement $n_{\mathrm{eq}} = 89\,\mathrm{fm}/\sqrt{\mathrm{Hz}}$ was obtained from fitting the first flexural mode thermal noise spectrum.

Figures 9(c) and (d) show the dependence of the force derivative noise on measurement bandwidth for the first and second flexural modes, respectively, for a rms oscillation amplitude of 100 pm and quality factors Q_1=100k and Q_2=10k. The measurement sensitivity of the first and second flexural cantilever mode are both limited by thermal noise for measurement bandwidths smaller than 18 Hz and 22 Hz, respectively, and by deflection noise for larger bandwidths. However, for bandwidths up to 100 Hz, the noise remains below 1 mN/m even for the second flexural mode and below 0.1 mN/m for bandwidths smaller than about 22 Hz, as typically used in tuning fork AFM experiments. About an order of magnitude better sensitivities are then obtained in the first cantilever oscillation mode. Note that these values are obtained for a non-optimized interferometer with a noise floor of $89\,\mathrm{fm}/\sqrt{\mathrm{Hz}}$ [Fig. 9(a)], clearly demonstrating the superior performance possible with cantilever-based AFM.

For comparison, the dependence of the minimally-measurable force derivatives for an MFM cantilever [29] with $f_1 = 51.002\,\mathrm{kHz}$, $k_1 = 0.86\,\mathrm{N/m}$, and $Q_1 = 241.908\mathrm{k}$ obtained at room temperature (solid lines) and 6.4 K (dashed lines) are displayed in Fig. 9(e) for a rms oscillation amplitude of 5 nm (as typically used for MFM [29]). The sensitivity of the softer MFM cantilever (operated at a 50 times larger oscillation amplitude compared to the one used in the second flexural mode) is considerably higher than that of the hard cantilever (note that the scale is given in μN/m instead of mN/m) and not limited by detector noise at room temperature. Such an extremely high force derivative sensitivity is key for MFM experiments with high spatial resolution (and also to minimize the influence of the tip stray field on the sample by employing low magnetic moment tips). In addition, such a sensitivity is also useful for mapping other small forces, such as weak electrostatic, van der Waals or Casimir forces, highlighting the advantages arising from using cantilevers with force constant optimized for a particular type of tip-sample interaction. At 6.4 K the total noise of the MFM cantilever is again limited by detector noise for bandwidths above 50 Hz. The noise of the deflection sensor employed here is clearly relevant for measurements performed at higher bandwidths at low temperatures for all types of cantilevers. Best interferometer optical sensors have been reported to reach measurement sensitivities of better than 1 fm/$\sqrt{\text{Hz}}$ [47,48], a sensitivity not achieved here for our interferometer that still employs an uncoated fiber end. The sensitivities which could be obtained with such improved interferometer setups are displayed in Figs. 9(f)-(h) for measurement bandwidths up to 2 kHz. Clearly, the deflection sensor noise does no longer limit the minimally-detectable force derivative for bandwidths up to and beyond 1 kHz. Such high measurement bandwidths can for example, be used to measure with high speed a large scale image showing atomic steps of the Au(111) surface with thin NaCl islands on top (see section VI). As discussed in section I, there is third noise source, the oscillator noise given by eq. 3, that is however relevant only for low-quality factor conditions [57]. An experimental evaluation of the measured frequency shift noise revealed that it depends as $B^{\frac{3}{2}}$ on the bandwidth B, confirming that the relevant noise source with our current interferometer sensor is the deflection noise and that the oscillator noise remains negligible(as expected for high-quality factor conditions). Consequently, the high resonance frequency to stiffness ratio of microfabricated cantilevers is highly advantageous for AFM measurements with the highest sensitivity or for more rapid scanning, requiring larger measurement bandwidths (see table 1).

STM noise spectrum and tip-sample gap stability measurements

A scanning probe microscopy tool designed for the acquisition of data with atomic resolution requires a tip-sample gap stability that is in the best case better than 1 pm. A convenient method to test the gap stability is to measure the current noise while tunneling on a conducting sample. Figure 10 displays the current noise spectrum up to 1600 Hz for the tip retracted from the surface (wide gray line) and for the tip approached to the surface (thin black line) such that a tunnel current of 20 pA is obtained with a bias of 200 mV, respectively. The noise spectrum (left vertical scale) recorded with the tip retracted from the surface contains a few peaks, which we attribute to triboelectric currents arising from mechanical vibrations of the cables running along the cryostat, but all peaks remain smaller than 45 fArms/$\sqrt{\text{Hz}}$.

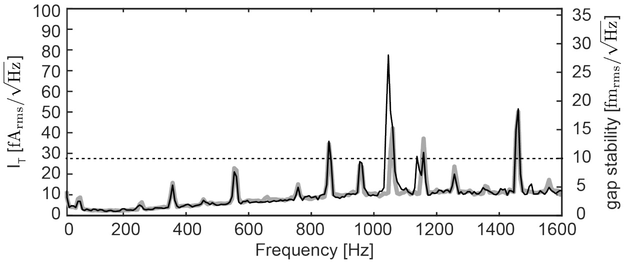

Figure 10: The current noise spectral density with the tip retracted from and approached to the surface of an electrically conducting sample between measurement bandwidth of 0 to 1600 Hz. The current noise spectral density with the retracted tip is displayed as a wide gray curve with a current noise in the left vertical scale. The current noise spectral density with the approached tip is displayed as a solid black line with a tunneling current noise in the left vertical scale and with a converted noise of the tip-sample gap stability in the right vertical scale. The dashed horizontal black line indicates a noise level of 10 fm/$\sqrt{\text{Hz}}$.

If the tip is tunneling, the background noise and most peaks remain unchanged, apart from the peak at 1.05 kHz that becomes noticeably larger, i.e. doubles from about 40 to 80 fA/$\sqrt{\text{Hz}}$. We attribute this increased noise to the thermal noise of the scan piezo that has its first resonance in this frequency range for a Au single crystal sample mounted on a button heater sample holder [Fig. 7(a)-(c)]. Using previously-measured tunneling current versus sample z-displacement data (not shown), the tunneling current noise data (solid black line in Fig. 10 and left vertical axis) can be converted into displacement noise or noise of the tip-sample gap stability (displayed by the right vertical scale in Fig. 10). The largest noise at about 1.05 kHz then is about 35 $\text{fm}_{\text{rms}}/\sqrt{\text{Hz}}$. The average noise for the whole spectrum remains below about 10 $\text{fm}_{\text{rms}}/\sqrt{\text{Hz}}$ (dashed horizontal black line in Fig. 10). Consequently, the integrated rms-noise up to a 1600 Hz bandwidth remains smaller than 400 fm, which permits measurements of sub-pm corrugations as observed for the atomic resolution image on Au(111) performed with an CO-functionalized tunneling tip at a tunnel-current setpoint of 30 pA and a bias of 5 mV [Fig. 11(f)].

EXPERIMENTAL RESULTS

STM Measurements

Figure 11(a) and (b) show an STM image and cross-section [taken at the location of the blue line in (a)], respectively, of a Au(111) surface acquired at 600 mV and 20 pA. A step and the herringbone structure are well visible.

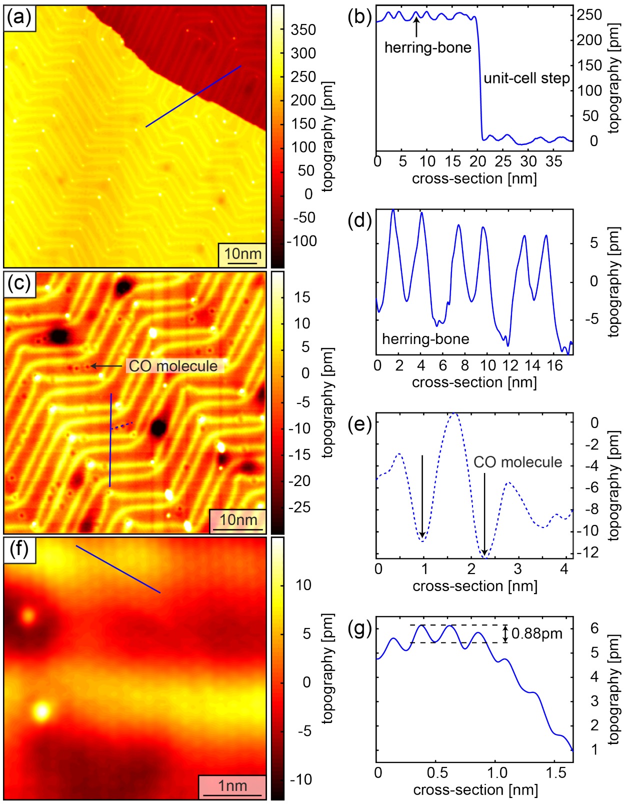

Figure 11: (a) and (c) STM results on Au(111) obtained at 600 mV and 20 pA. (b), (d) and (e) cross-sections taken at the locations of the solid blue lines in (a), (c) and the dashed blue line in (c). (f) atomic resolution image acquired at 5 mV and 30 pA. The cross-section (g) taken at the location of the blue line in (f) shows an atomic corrugation of only 0.88 pm.

Figure 11(c) and (d) show a smaller scan area and cross-section acquired on one terrace. Some CO was dosed onto the surface for a successive tip functionalization. The CO molecules appear as dark spots in the image (black arrow). The cross-section from Fig. 11(e) taken at the location of the blue dashed line in panel (c) shows that the CO molecules appear as about 8-10 pm deep depressions. Panel (f) then shows a smaller image acquired at 5 mV and 30 pA, where the herringbone structure is visible together with the atoms. We attribute the extremely small atomic corrugation of less than

1 pm [Fig. 11(g)], to the relatively low current setpoint and to the CO functionalized tip. Nevertheless, corrugations of less than 1 pm can be detected, confirming the excellent tip-sample gap stability of our instrument compatible with that assessed from the tunnel current noise analysis [Fig. 10].

Rapid scanning and atomic resolution

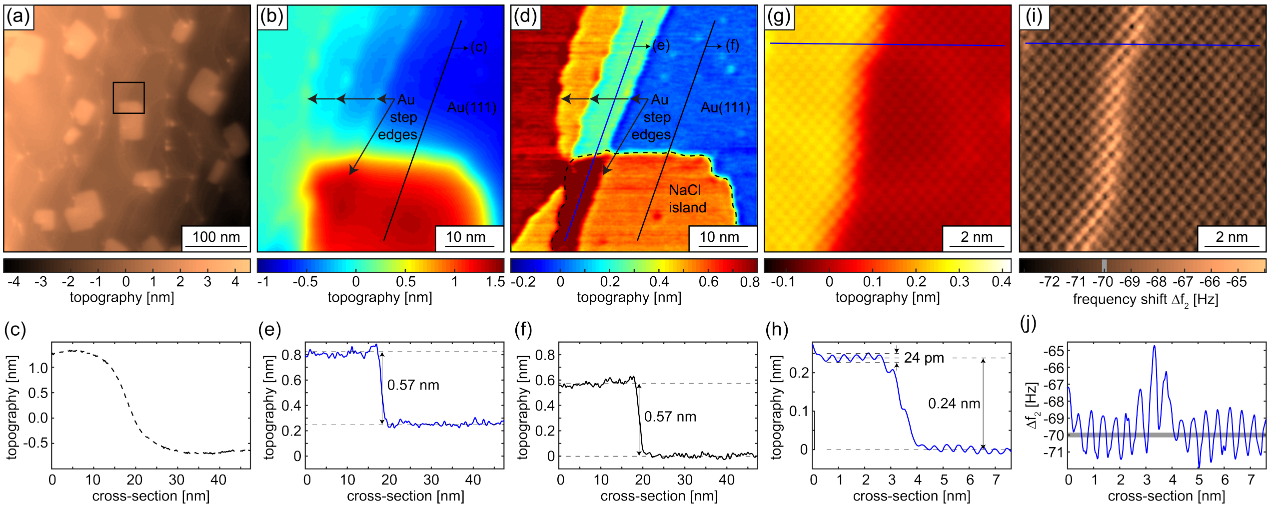

Figure 12: (a) 400 × 400 nm^2-image of NaCl islands on a Au(111) surface scanned with the cantilever operated in its first flexural oscillation mode with an amplitude $A_{\mathrm{f1,rms}} = 2\,\mathrm{nm}$ and a small negative frequency shift setpoint $\Delta f_{\mathrm{f1}} = -15\,\mathrm{Hz}$, permitting image acquisition at relatively large tip-sample distance for rapid overview scanning. (b) and (d) smaller scale images acquired in the first and second cantilever oscillation mode operated with amplitudes $A_{\mathrm{f1,rms}} = 2\,\mathrm{nm}$ and $A_{\mathrm{f2,rms}} = 100\,\mathrm{pm}$, respectively, at the location of the black square in (a), with negative frequency shift set-points for the first and second flexural mode, $\Delta f_{\mathrm{f1,f2}} = -15\,\mathrm{Hz}$. Note that the NaCl islands [enclosed by the dashed line in (d)] runs over the lower Au(111) step edge. (c) cross-section taken at the location of the black line in (b). (e) and (f) cross-sections taken at the location of the blue and black line in panel (d), respectively. (g) Atomic resolution image and corresponding cross-section (h) of the NaCl islands running over the Au(111) step edge measured with the second flexural mode with an oscillation amplitude $A_{\mathrm{f2,rms}} = 100\,\mathrm{pm}$ and $\Delta f_{\mathrm{f2}} = -70\,\mathrm{Hz}$. (i) Frequency shift error image and corresponding cross-section (j).

As discussed in subsections A and B of section V and summarized in Table 1, microfabricated cantilevers have a small stiffness-to-resonance frequency ratio which improves the force derivative sensitivity substantially. Atomic resolution imaging with AFM is conveniently performed with oscillation amplitudes that are comparable to the decay length of the short-range inter-atomic forces [67]. A stable operation of the PLL with such small oscillation amplitudes requires a cantilever stiffness of a few hundred N/m, such that sufficient energy is stored in the cantilever oscillation [61], i.e.:

$$\frac{1}{2}k_i \cdot A_i^2 \gg \Delta E \ , \tag{12}$$

where k_i and A_i are the cantilever stiffness and oscillation amplitude, respectively, of the oscillation mode i. ΔE is a typical energy loss that can stochastically occur, for example, if the position of an atom within the tip-sample force field becomes instable [68,69]. Such stochastic energy loss processes lead to sudden changes of the phase which cause the PLL to unlock and consequently to a crash of the z-feedback, which is set up to keep the frequency shift constant.

For oscillation amplitudes below 100 pm, eq. 12 reveals that a stiffness above 100 N/m is required for $\Delta E \sim 1$ eV. According to eq. 5, such a cantilever stiffness is conveniently obtained with the second flexural oscillation mode of a cantilever with a first mode stiffness larger than about 10 N/m. Operated in its first flexural mode, such a cantilever then obtains a force derivative sensitivity of better than 0.12 mN/m for a bandwidth of 100 Hz [Fig. 9(c)]. Increasing the first mode oscillation amplitude to 2 nm then provides such a sub-mN/m sensitivity even for PLL bandwidths of 2 kHz. These high bandwidths therefore permit the rapid scanning of large sample areas, which is convenient for finding a specific are of interest, for example, on a device, that will later be scanned with atomic resolution.

Here, we thermally evaporate sub-monolayer NaCl onto a Au(111) surface to obtain a sample surface with different step heights, making large-scale AFM imaging with higher scan rates challenging. The contact potential on the Au was compensated by application of a bias of 828 mV. To acquire AFM overview images and then atomic resolution images at selected surface locations, including lateral force measurements, we advantageously used the different oscillation modes of a commercial 40 N/m cantilever with first, second flexural and first torsional mode resonance frequencies of 289 kHz, 1829 kHz, and 2178 kHz, respectively.

Figure 12(a) displays a $400 \times 400\,\mathrm{nm}^2$-image of NaCl islands on a Au(111) surface scanned at 500 ms per line with 256 pixels, a PLL bandwidth of 500 Hz was used for a frequency shift kept constant at -15 Hz. Figure 12(b) then shows a zoomed scan at the location of black square in

Fig. 12(a). Note that the step edge [see cross-section displayed in Fig. 12(c)] appears very rounded and the step height is much higher than that expected for two monolayers of NaCl. These observations can be attributed to the relatively large first mode oscillation amplitude (2 nm) and small negative frequency shift setpoint such that the frequency shift predominately arises from longer ranged van der Waals and electrostatic forces and, consequently, a constant frequency shift image does not reflect the true sample topography.

An AFM image acquired at the same location, but using the second flexural mode with an oscillation amplitude of 100 pm, again for a frequency shift setpoint of -15 Hz is displayed in Fig. 12(d) with the cross-sections taken at the blue and black lines depicted in Fig. 12(e) and (f). The comparison of the step heights of the two cross-sections reveals that the NaCl island grows over a unit cell step of the Au(111) surface. Because the second flexural oscillation mode of the cantilever is now used, which has an about 40× higher modal stiffness (eq. 5), the tip-sample interaction force gradient averaged over the oscillation path of the tip is correspondingly larger, while the tip-sample distance is reduced. Moreover, because the oscillation amplitude is reduced from 2 to 0.1 nm, the contribution of the short range force to the frequency shift is considerably larger. Hence, changes of the (long range) electrostatic force arising from local contact potential variations have a reduced effect on the frequency shift and thus on the measured topography. Consequently, the edge of the NaCl island appears much sharper than in the image Fig. 12(b) acquired with the first flexural oscillation mode and the observed step height of about 0.57 nm; this value corresponds well to the unit cell lattice constant of NaCl of 0.538 nm, i.e. for two monolayers of NaCl [70].

For atomic resolution imaging, the tip was CO-functionalized on the Au surface which change the contact potential substantially such that the bias had to be reduced from 828 mV to -28 mV. Fig. 12(g) was acquired using a more negative frequency shift kept constant at -70 Hz on a $9 \times 9\,\mathrm{nm}^2$ selected inside the NaCl islands covering a Au(111) step edge. As visible in the cross-section displayed in Fig. 12(h), the observed step height of 0.24 nm corresponds to that of a monolayer step of the Au(111) surface, and the atomic scale periodicity is about 0.5 nm, less than the bulk lattice constant of 0.538 nm, as expected for a thin 2D NaCl sheets [70]. Fig. 12(i) and (j) show the frequency shift (error) image and cross-section, respectively. The atomic scale corrugation of 24 pm [Fig. 12(h)] leads to a frequency shift error of ±1 Hz around the frequency shift setpoint of -70 Hz, while the Au step leads to a lager frequency shift error of about -5 Hz [Fig. 12(j)]. Apart from using different flexural cantilever oscillation modes for rapid large scale and local atomic resolution imaging, the cantilever can also be oscillated on its torsional modes, permitting the measurement of lateral forces or multimodal operation of flexural and torsional oscillation modes [34,35,71]. Here, we demonstrate that positioning the fiber-end of the interferometric deflection sensor outside the cantilever long axis, close to its edges[Fig. 8(e)], the torsional cantilever oscillation mode can be measured simultaneously with the flexural ones [Fig. 8(d) and (f)]. Similar to the work of Kawai et al.[36], we operate the z-feedback on the second flexural mode frequency to control the tip-sample distance, while simultaneously imaging the frequency shift of the first torsional mode to map the lateral tip-sample force derivative (along the torsional oscillation axis of the tip), or alternatively use the tunnel current for the z-feedback. Figure 13(a) displays a $4 \times 4\,\mathrm{nm}^2$-topography image of a NaCl island overgrowing a step edge of the Au(111) surface. The data was acquired with a second flexural mode frequency shift Δf_{f2} kept constant at -90 Hz and an oscillation amplitude $A_{\mathrm{f2,rms}} = 100$ pm, while Fig. 13(b) shows the simultaneously measured tunnel current image obtained for a bias of 100 mV. The blue lines in Fig. 13(c) and (d) display cross-sectional data of the topography (a) and tunnel current (b) images, respectively. Interestingly, the current drops to a minimum of about 55 pA when the tip scans from the upper to the lower terrace, indicating that the tip is a bit farther away from the surface in the vicinity of the step edge. This is because a part of the mesoscopic tip is still located above the upper terrace contributing to an increased negative Δf_{f2}. Only if the tip moves farther away from the step edge, the average tunnel current and the tunnel current corrugation level recover to the value measured away from the step edge on the upper terrace. From larger scale images (not shown) we can conclude that size of the tip apex must have a diameter smaller than about 15 nm. If the cantilever is additionally driven on the first torsional mode with an amplitude $A_{\mathrm{t1,rms}} = 60$ pm, the atomic resolution in the topography image from Fig. 13(e) and cross-section displayed as green line in Fig. 13(c) is still visible, but reduced considerably. The difference data displayed in in Fig. 13(g) and the corresponding cross-sectional data Fig. 13(i) reveal that the contrast reduction is most significant at the step edge. Atomic resolution was also obtained in the torsional frequency shift Δf_{t1}-data shown in Fig. 13(h). As already observed by Kawai et al.[36], a strong negative torsional frequency shift appears as the tip approaches to the step from the lower terrace side, which must arise from a rather strong attractive lateral force towards the step edge. The dashed line (in Fig. 13(j)) shows the result of a fit in the cross-section interval [1.26 nm, 4.255 nm] of two exponential decay functions with wavelengths fixed at $\lambda_1 = 3.6\,\mathrm{nm}$ and $\lambda_2 = 0.5\,\mathrm{nm}$, corresponding to the Fermi wavelength of the Au(111) free electron like surface state [72], and NaCl ion periodicity, respectively. This indicates that the lateral force may arise from a charge on the step edge of the Au(111) and a contribution from the periodic charges of the ionic lattice. On the upper side the atomic corrugation is also visible but in contrast to Kawai *et al.*, no overall attractive force (negative torsional frequency shift is visible).

Atomic resolution images can be obtained with different z-feedback input signals. Figure 13(b) shows the tunnel current data obtained with the second mode flexural frequency $\Delta f_{\mathrm{f2}} = -90\,\mathrm{Hz}$. The Δf_{f2} error signal data shown in Fig. 13(k) reveals that the frequency shift is kept within about ±1 Hz. Correspondingly, Fig. 13(l) shows the second mode flexural frequency data if the tunnel current is kept at 100 pA [Fig. 13(m) is the corresponding current error data]. Panels (n) and (o) then show cross-sectional data for the two feedback setups.

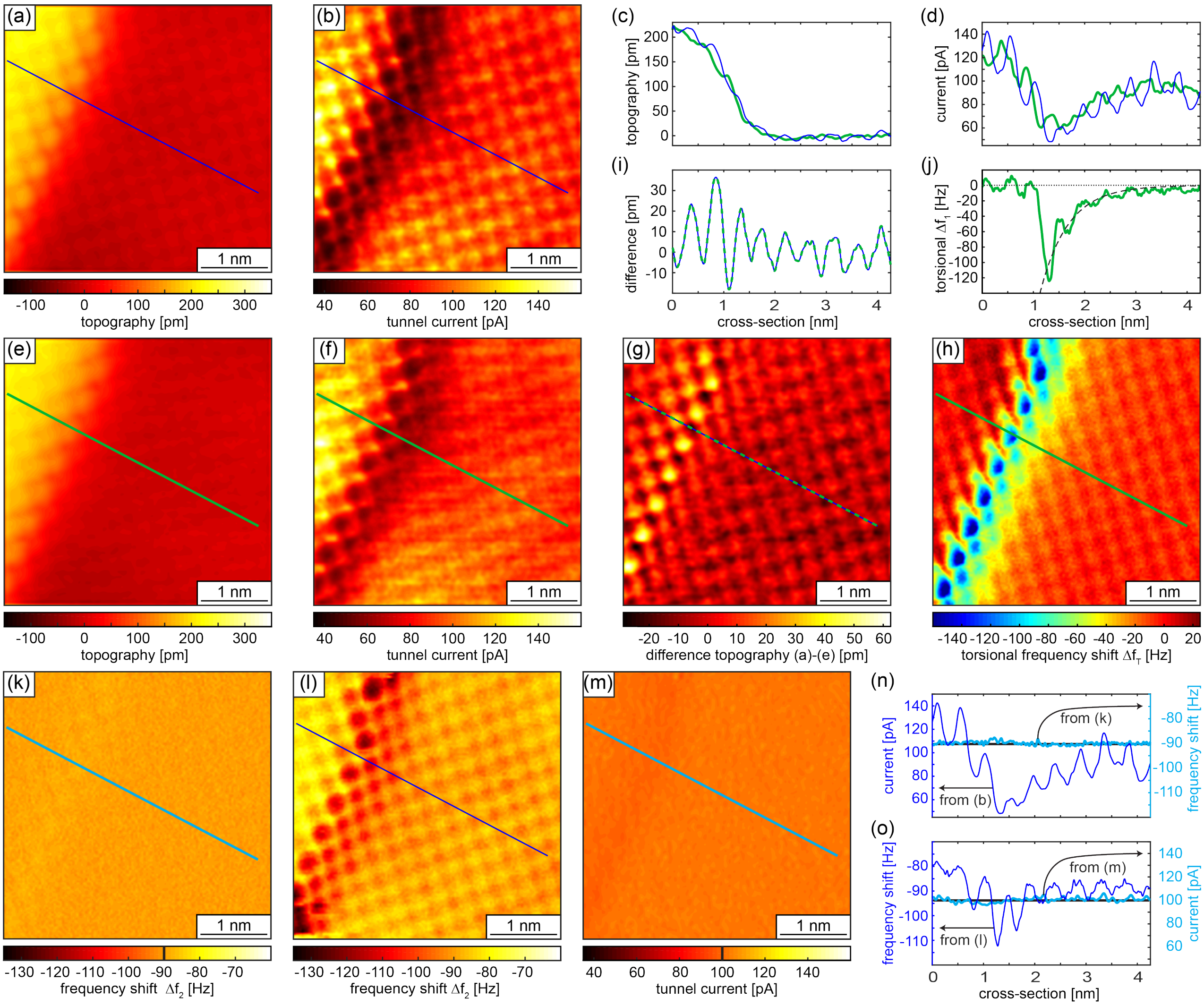

Figure 13: Multi-channel and multimodal AFM results obtained on a NaCl island running over an Au(111) step edge. (a) topography and (b) tunnel current images obtained with the second flexural mode frequency shift $\Delta f_{f2} = -90\,\mathrm{Hz}$ and a second mode oscillation amplitude $A_{f2,rms} = 100\,\mathrm{pm}$. The blue lines in panels (c) and (d) represent the cross-sections taken at the location of the blue lines in (a) and (b), respectively. (e) and (f) show the same quantities as (a) and (b) but with the cantilever oscillated simultaneously in its first torsional mode with a torsional mode amplitude $A_{t1,rms} = 60\,\mathrm{pm}$ to obtain the torsional mode frequency shift image $\Delta f_{t1}(x, y)$ displayed in panel (h). A large lateral attractive force is observed if the tip is approached to the step edge from the lower terrace side. See green cross-section in (j). Because of the additional lateral tip oscillation, the topographical corrugation in (e) is slightly reduced compared to that in (a). Compare also the topography and tunnel current cross-sections, i.e. green and blue lines in panel (c) and (d), respectively. The reduction of the topographical corrugation is particularly pronounced at the step edge as visible in the difference data displayed in (g) calculated by subtracting the data shown in (a) from that displayed in (e). (i) shows the green dashed cross-section in (g). (k) displays the frequency shift error observed during the constant frequency shift imaging used for the data displayed in (a) and (b). Alternatively, the tunnel current can be kept constant. Then the frequency shift shows an atomic scale contrast (l). The corresponding tunnel current error image is displayed in (m). (n) and (o) show the tunnel current and frequency shift variations along the cross-sections indicated by the lines in (b) and (l), respectively, while the frequency shift or tunnel current is kept constant [pale blue lines in (n) and (o)].

Summary and Conclusions

In this article, we have described the design and construction of a cantilever-based low temperature UHV AFM with sub-picometer gap stability that enables multimodal and multidimensional AFM operation combined with STM. The use of microfabricated cantilevers requires the implementation of an additional deflection sensor which increases the complexity of the instruments but the low ratio of the stiffness to resonance frequency (stemming from the small geometrical dimensions of cantilevers) significantly reduces thermal and deflection noise force derivatives. Because the latter is often the dominating noise source (particularly for tuning fork-based AFM instrumentation), the cantilever-based AFM instrument presented here has a two orders of magnitude increased force derivative sensitivity, permitting high AFM measurement bandwidths typically of a few hundred Hz (and which could be further increased to 2 kHz with improved interferometric detection [47,48]). Further, because a larger variety of cantilevers with a large stiffness range are available, cantilevers optimized for a special experimental task can be used, e.g. for magnetic force microscopy with the highest field sensitivity [29] or atomic resolution work (as shown here). In addition, microfabricated cantilevers permit multimodal operation, for example for magnetic force microscopy with capacitive tip-sample distance control [33], or the simultaneous mapping of vertical and lateral forces and the tunnel current with atomic scale resolution as demonstrated here. Future scientific frontiers may require an AFM-based search on a micron scale over device structures including insulating parts and thus requiring an AFM imaging tool that can accomplish large area scans using weak van der Waals forces and thus with a relatively large tip-sample distance permitting robust overview scanning.

Acknowledgments

We acknowledge financial support from the SNF project *Stochastic Atomic and Molecular Fluctuators and Resonators* Grant number 200021_175726, EU FP 7 project *MDSPM* Grant agreement 214250, and from Empa.

References

1. Kirk, M. D.; Albrecht, T. R.; Quate, C. F. *Review of Scientific Instruments* **1988**, *59* (6), 833–835.

2. Metz, V.; Raanan, H.; Pieper, H.; Bosbach, D.; Ganor, J. *Geochimica et Cosmochimica Acta* **2005**, *69* (10), 2581–2591. doi:https://doi.org/10.1016/j.gca.2004.11.009.

3. Schulz, F.; Maillard, J.; Kaiser, K.; Schmitz-Afonso, I.; Gautier, T.; Afonso, C.; Carrasco, N.; Gross, L. *The Astrophysical Journal Letters* **2021**, *908* (1), L13. doi:10.3847/2041-8213/abd93e.

4. Giessibl, F. J. *Science* **1995**, *267* (5194), 68–71.

5. Ueyama, H.; Ohta, M.; Sugawara, Y.; Morita, S. *Japanese Journal of Applied Physics* **1995**, *34* (Part 2, No. 8B), L1086–L1088.

6. Kitamura, S.; Iwatsuki, I. M. *Japanese journal of applied physics* **1995**, *34* (1B), L145.

7. Sugawara, Y.; Ohta, M.; Ueyama, H.; Morita, S. *Science* **1995**, *270* (5242), 1646–1648.

8. Gross, L.; Mohn, F.; Moll, N.; Liljeroth, P.; Meyer, G. *Science* **2009**, *325* (5944), 1110–1114.

9. Alldritt, B.; Urtev, F.; Oinonen, N.; Aapro, M.; Kannala, J.; Liljeroth, P.; Foster, A. S. *Computer Physics Communications* **2022**, *273*, 108258.

10. Mönig, H.; Hermoso, D. R.; Díaz Arado, O.; Todorović, M.; Timmer, A.; Schüer, S.; Langewisch, G.; Pérez, R.; Fuchs, H. *ACS nano.* **2016-01-26**, *10* (1), year.

11. Mohn, F.; Schuler, B.; Gross, L.; Meyer, G. *Applied Physics Letters* **2013**, *102* (7), 073109.

12. Giessibl, F. J. *Review of Scientific Instruments* **2019**, *90* (1), 011101.

13. Schwenk, J.; Kim, S.; Berwanger, J.; Ghahari, F.; Walkup, D.; Slot, M. R.; Le, S. T.; Cullen, W. G.; Blankenship, S. R.; Vranjkovic, S.; Hug, H. J.; Kuk, Y.; Giessibl, F. J.; Stroscio, J. A. *Review of Scientific Instruments* **2020**, *91* (7), 071101.

14. Albers, B. J.; Schwendemann, T. C.; Baykara, M. Z.; Pilet, N.; Liebmann, M.; Altman, E. I.; Schwarz, U. D. *Nature Nanotechnology* **2009**, *4* (5), 307–310.

15. Garcia, R.; Herruzo, E. T. *Nature nanotechnology* **2012**, *7* (4), 217–226.

16. Platz, D.; Tholén, E. A.; Pesen, D.; Haviland, D. B. *Applied Physics Letters* **2008**, *92* (15), 153106 –4.

17. Li, J. W.; Cleveland, J. P.; Proksch, R. *Applied Physics Letters* **2009**, *94* (16), 163118–4.

18. Dietz, C.; Herruzo, E. T.; Lozano, J. R.; Garcia, R. *Nanotechnology* **2011**, *22* (12), 125708.

19. Forchheimer, D.; Platz, D.; Tholén, E. A.; Haviland, D. B. *Physical Review B* **2012**, *85* (19), 195449 –7.

20. Forchheimer, D.; Platz, D.; Tholén, E. A. *Applied Physics Letters* **2013**, *103*, 013113.

21. Nievergelt, A. P.; Adams, J. D.; Odermatt, P. D.; Fantner, G. E. *Beilstein Journal of Nanotechnology* **2014**, *5* (1), 2459–2467.

22. Nievergelt, A. P.; Erickson, B. W.; Hosseini, N.; Adams, J. D.; Fantner, G. E. *Scientific Reports* **2015**, 1–12.

23. Penedo, M.; Hug, H. J. *Applied Physics Letters* **2018**, *113* (2), 023103–6.

24. Braunsmann, C.; Schäffer, T. E. *Nanotechnology* **2010**, *21* (22), 225705.

25. Young, T. J.; Monclus, M. A.; Burnett, T. L.; Broughton, W. R.; Ogin, S. L.; Smith, P. A. *Measurement Science & Technology* **2011**, *22* (12), 125703–7.

26. Collins, L.; Belianinov, A.; Proksch, R.; Zuo, T.; Zhang, Y.; Liaw, P. K.; Kalinin, S. V.; Jesse, S. *Applied Physics Letters* **2016**, *108* (19), 193103. Publisher: American Institute of Physics

27. Kalinin, S. V.; Strelcov, E.; Belianinov, A.; Somnath, S.; Vasudevan, R. K.; Lingerfelt, E. J.; Archibald, R. K.; Chen, C.; Proksch, R.; Laanait, N.; Jesse, S. *ACS Nano* **2016**, *10* (10), 9068–9086. Publisher: American Chemical Society

28. Rugar, D.; Stipe, B.; Mamin, H.; Yannoni, C.; Stowe, T.; Yasumura, K.; Kenny, T. *Applied Physics A* **2001**, *72* (1), S3–S10.

29. Feng, Y.; Vaghefi, P. M.; Vranjkovic, S.; Penedo, M.; Kappenberger, P.; Schwenk, J.; Zhao, X.; Mandru, A.-O.; Hug, H. *Journal of Magnetism and Magnetic Materials* **2022**, *551*, 169073.

30. Schwenk, J.; Marioni, M.; Romer, S.; Joshi, N. R.; Hug, H. J. *Applied Physics Letters* **2014**, *104* (11), 112412. Publisher: American Institute of Physics

31. Schwenk, J.; Zhao, X.; Bacani, M.; Marioni, M. A.; Romer, S.; Hug, H. J. *Applied Physics Letters* **2015**, *107* (13), 132407. Publisher: American Institute of Physics

32. Zhao, X.; Schwenk, J.; Mandru, A. O.; Penedo, M.; Bacani, M.; Marioni, M. A.; Hug, H. J. *New Journal of Physics* **2018**, *20* (1), 013018. Publisher: IOP Publishing

33. Zhao, X.; Schwenk, J.; Mandru, A.; Penedo, M.; Baćani, M.; Marioni, M.; Hug, H. *New Journal of Physics* **2018**, *20* (1), 013018.

34. Pfeiffer, O.; Bennewitz, R.; Baratoff, A.; Meyer, E.; Grütter, P. *Physical Review B* **2002**, *65* (16), 319 –4.

35. Kawai, S.; Kitamura, S.-i.; Kobayashi, D.; Kawakatsu, H. *Applied Physics Letters* **2005**, *87* (17), 173105.

36. Kawai, S.; Canova, F. F.; Glatzel, T.; Hynninen, T.; Meyer, E.; Foster, A. S. *Physical Review Letters* **2012**, *109* (14), 146101.

37. Kawai, S.; Glatzel, T.; Koch, S.; Such, B.; Baratoff, A.; Meyer, E. *Phys. Rev. B* **2010-02**, *81* (8), 085420.

38. Kawai, S.; Pina, C. M.; Bubendorf, A.; Fessler, G.; Glatzel, T.; Gnecco, E.; Meyer, E. *Nanotechnology* **2013**, *24* (5), 055702.

39. Kawai, S.; Pawlak, R.; Glatzel, T.; Meyer, E. *Phys. Rev. B* **2011**, *84*, 085429.

40. The UHV chambers and cryosystem were fabricated by Createc GmbH which is a modified version of their UHV low temperature STM.

41. CryoVac GmbH & Co. KG, D-53842 Troisdorf, Germany.

42. PH BRONZE 5% CDA 510 A, California Fine Wire Co., CA 93433, USA.

43. Meyer, G.; Amer, N. M. *Applied Physics Letters* **1988**, *53* (12), 1045–1047.

44. Rugar, D.; Mamin, H.; Guethner, P. *Applied Physics Letters* **1989**, *55* (25), 2588–2590.

45. Moser, A.; Hug, H.; Jung, T.; Schwarz, U.; Guntherodt, H.-J. *Measurement Science and Technology* **1993**, *4* (7), 769.

46. Hug, H. J.; Stiefel, B.; Van Schendel, P.; Moser, A.; Martin, S.; Güntherodt, H.-J. *Review of Scientific Instruments* **1999**, *70* (9), 3625–3640.

47. Hoogenboom, B. W.; Frederix, P. L. T. M.; Yang, J. L.; Martin, S.; Pellmont, Y.; Steinacher, M.; Zäch, S.; Langenbach, E.; Heimbeck, H.-J.; Engel, A.; Hug, H. J. *Applied Physics Letters* **2005**, *86* (7), 074101. Publisher: American Institute of Physics

48. Karc, Ö.; Çelik, Ü.; Oral, A. *Review of Scientific Instruments* **2020**, *91* (1), 013703. doi:10.1063/1.5120007.

49. Pan, S.; Hudson, E. W.; Davis, J. *Review of scientific instruments* **1999**, *70* (2), 1459–1463.

50. Hug, H. J.; Stiefel, B.; van Schendel, P. J. A.; Moser, A.; Hofer, R.; Martin, S.; Güntherodt, H.-J.; Porthun, S.; Abelmann, L.; Lodder, J. C.; Bochi, G.; O'Handley, R. C. *Journal of Applied Physics* **1998**, *83* (11), 5609–5620.

51. SS coaxial cable, CC-SS-100, Lake Shore Cryotronics, Inc., Woburn, MA 01801, USA.

52. 2451 DAFLON Microminiature PTFE Coated Hook-Up Wire,Daburn Electronics & Cable., Dover, NJ 07801, USA.

53. Special production done by SFK Schulz GmbH, 12555 Berlin, Germany .

54. Thorlabs GmbH (Lübeck), 23562 Lübeck, Germany .

55. Reinstaedtler, M.; Rabe, U.; Scherer, V.; Turner, J. A.; Arnold, W. *Surface Science* **2003**, *532-535*, 1152–1158. Proceedings of the 7th International Conference on Nanometer-Scale Science and Technology and the 21st European Conference on Surface Science

56. Kawai, S.; Glatzel, T.; Hug, H.-J.; Meyer, E. *Nanotechnology* **2010**, *21* (24), 245704. doi:10.1088/0957-4484/21/24/245704.

57. Kobayashi, K.; Yamada, H.; Matsushige, K. *Review of Scientific Instruments* **2009**, *80* (4), 043708.

58. Butt, H. J.; Jaschke, M. *Nanotechnology* **1995**, *6* (1), 1–7.

59. Morita, S.; Giessibl, F. J.; Meyer, E.; Wiesendanger, R. *Noncontact Atomic Force Microscopy: Volume 3*; Springer, 2015.

60. Lübbe, J.; Tröger, L.; Torbrügge, S.; Bechstein, R.; Richter, C.; Kühnle, A.; Reichling, M. *Measurement Science and Technology* **2010**, *21* (12), 125501. Publisher: IOP Publishing

61. Giessibl, F. J.; Hembacher, S.; Herz, M.; Schiller, C.; Mannhart, J. *Nanotechnology* **2004**, *15* (2), S79 –S86.

62. Kirpal, D.; Qiu, J.; Pürckhauer, K.; Weymouth, A. J.; Metz, M.; Giessibl, F. J. *Review of Scientific Instruments* **2021**, *92* (4), 043703.

63. Hölscher, H.; Milde, P.; Zerweck, U.; Eng, L. M.; Hoffmann, R. *Applied Physics Letters* **2009**, *94* (22), 223514.

64. Cohadon, P.-F.; Heidmann, A.; Pinard, M. *Physical Review Letters* **1999**, *83* (16), 3174.

65. Metzger, C.; Ludwig, M.; Neuenhahn, C.; Ortlieb, A.; Favero, I.; Karrai, K.; Marquardt, F. *Physical review letters* **2008**, *101* (13), 133903.

66. Adiga, V. P.; Sumant, A. V.; Suresh, S.; Gudeman, C.; Auciello, O.; Carlisle, J. A.; Carpick, R. W. *Phys. Rev. B* **2009**, *79*, 245403.

67. Giessibl, F. J. *Reviews of Modern Physics* **2003-07**, *75* (3), 949 –983.

68. Hoffmann, R.; Baratoff, A.; Hug, H. J.; Hidber, H. R.; v Löhneysen, H.; Güntherodt, H.-J. *Nanotechnology* **2007**, *18* (39), 395503.

69. Ghasemi, S. A.; Goedecker, S.; Baratoff, A.; Lenosky, T.; Meyer, E.; Hug, H. J. *Physical Review Letters* **2008**, *100* (23), 236106.

70. Hebenstreit, W.; Redinger, J.; Horozova, Z.; Schmid, M.; Podloucky, R.; Varga, P. *Surface Science* **1999**, *424*, L321.

71. Kawai, S.; Glatzel, T.; Koch, S.; Such, B.; Baratoff, A.; Meyer, E. *Phys. Rev. Lett.* **2009-11**, *103* (22), 220801.

72. Sotthewes, K.; Nijmeijer, M.; Zandvliet, H. J. W. *Phys. Rev. B* **2021**, *103*, 245311.